



1 Long-term monitoring (1953-2019) of geomorphologically active 2 sections on LIA lateral moraines under changing meteorological 3 conditions

4 Moritz Altmann¹, Madlene Pfeiffer², Florian Haas¹, Jakob Rom¹, Fabian Fleischer¹, Tobias Heckmann¹,
5 Livia Piermattei^{1,3}, Michael Wimmer⁴, Lukas Braun⁵, Manuel Stark¹, Sarah Betz-Nutz¹, Michael Becht¹

6 ¹Department of Physical Geography, Catholic University of Eichstätt-Ingolstadt, Eichstätt, 85072, Germany

7 ²Institute of Geography, University of Bremen, Bremen, 28359, Germany

8 ³Swiss Federal Institute for Forest, Snow and Landscape Research (WSL), Birmensdorf, 8903, Switzerland

9 ⁴Department of Geodesy and Geoinformation, TU Wien, Vienna, 1040, Austria

10 ⁵Institute of Mathematics, Albert Ludwig University of Freiburg, Freiburg, 79104, Germany

11 *Correspondence to:* Moritz Altmann (MAltmann@ku.de)

12 **Abstract.** We show a long-term erosion monitoring of several geomorphologically active gully systems on Little Ice Age
13 lateral moraines in the central Eastern Alps covering a total time period from 1953 to 2019 including several survey periods
14 in order to identify corresponding morphodynamic trends. For the implementation, DEM of Differences were calculated based
15 on multitemporal high-resolution digital elevation models from historical aerial images (generated by structure-from-motion
16 photogrammetry with multi-view-stereo) and light detection and ranging from airborne platforms. Two approaches were
17 implemented to achieve the corresponding objectives. First, by calculating linear regression models using the accumulated
18 sediment yield and the corresponding catchment area (on a log-log scale), the range of the variability of the spatial distribution
19 of erosion values within the areas of interest is shown. Secondly, we use volume calculations to determine the total/mean
20 sediment output (and erosion rates) of the entire areas of interest. Subsequently, a comparison is made between the areas of
21 interest and the epochs of both approaches. Based on the slopes of the calculated regression lines, it could be shown that the
22 highest range of the variability of sediment yield within all areas of interest is in the first epoch (mainly 1950s to 1970s), as in
23 some areas of interest sediment yield per square metre increases clearly more (regression lines with slopes up to 1.5), which
24 in the later epochs (1970s to mid-2000s and mid-2000s to 2017/2019) generally decreases in 10 out of 12 cases (regression
25 lines with slopes around 1). However, even in the areas of interest with an increase in the variability of sediment yield over
26 time, the earlier high variabilities are no longer reached. This means that the spatial pattern of erosion in the gully heads
27 changes over time as it becomes more uniform. Furthermore, using sediment volume calculations and corresponding erosion
28 rates, we show a generally decreasing trend in geomorphic activity (amount of sediment yield) between the different epochs
29 in 10 out of 12 areas of interest, while 2 areas of interest show an opposite trend where morphodynamics increase and remain
30 at the same level. Finally, we summarise the results of long-term changes in the morphodynamics of geomorphologically active
31 areas on lateral moraines by presenting the "sediment activity concept", which, in contrast to theoretical models, is based on
32 actually calculated erosion. The level of geomorphic activity depends strongly on the characteristics of the areas of interest,



33 such as size, slope length and slope gradient, some of which are associated with deeply incised gullies. It is noticeable that
34 especially areas with decades of dead ice influence in the lower slope area show high geomorphic activity. Furthermore, we
35 show that system-internal factors as well as the general paraglacial adjustment process have a greater influence on long-term
36 morphodynamics than changing external weather and climate conditions, which, however, had a slight impact mainly in the
37 last, i.e. most recent epoch (mid-2000s to 2017/2019) and may have led to an increase in erosion at the areas of interest.

38 **Keywords:** Airborne Laser Scanning (ALS), DEM of Difference (DoD), historical aerial images (HAI), gully erosion, Little
39 Ice Age (LIA) lateral moraines, modelling, Structure-from-Motion (SfM) photogrammetry, proglacial areas, Weather Research
40 and Forecasting (WRF) model

41 **1 Introduction**

42 Since the end of the Little Ice Age (LIA) around 1850 and the strong global warming of the last decades (IPCC, 2021; Pepin
43 et al., 2022), proglacial areas play a special role in the current landscape changes of high alpine geosystems, as such areas are
44 strongly increasing due to the ongoing retreat of the glaciers (Deline et al., 2015; Heckmann and Morche, 2019; Haerberli and
45 Whiteman, 2021). The melting of glaciers leads to the release of unstable sediment sources, which are subsequently exposed
46 to several geomorphological slope processes, which can lead to high erosion rates.

47 The relationship between this glacier melt and slope instability has been subject of research for several decades. Church and
48 Ryder (1972) were the first to develop a theoretical model (“paraglacial concept”) to describe future landscape change
49 throughout a proglacial area and defined the phase of transition as the paraglacial period, during which paraglacial processes
50 (non-glacial processes) occur. After a period of high geomorphic activity (fluvial erosion and transport) associated with a peak,
51 sediment production decreases over time until a “normal” level of sediment movement is reached. By further developing the
52 model, Ballantyne (2002a) describes this paraglacial landscape adjustment using the “sediment exhaustion model”, which is
53 based on a hypothetical paraglacial system. Several variable factors determine the duration of this period, such as sediment
54 release and the rate of sediment reworking. Following the sediment exhaustion model, the rate of sediment reworking of
55 glacial sediments in proglacial areas decreases exponentially if the sediment release rate only depends on sediment
56 availability (Ballantyne, 2002a, 2002b).

57 Ballantyne and Benn (1994) and Curry (1999) describe the paraglacial slope adjustment of lateral moraines by analysing the
58 formation of gully systems on lateral moraines and the corresponding alluvial fans and debris cones (both in western Norway).
59 These systems result from weathering and erosion, such as fluvial erosion, slope wash, debris flows, smaller slope failures,
60 and ground/snow avalanches (Ballantyne, 2002a, 2002b; Curry et al., 2006; Haas et al., 2012; Dusik et al., 2019). Material is
61 deposited in the gullies (e.g. by nival processes, fluvial activity and sidewall collapse) and is then transported downslope,
62 mainly by debris flows triggered in the gully heads after heavy rainfall or after rapid snowmelt (Ballantyne and Benn, 1994;
63 Ballantyne, 2002b; Curry et al., 2006). Similarly, large deformations such as deep-seated slope failures and landslides with
64 low frequency and high magnitude also occur (Mattson and Gardner, 1991; Blair, 1994; Hugenholtz et al., 2008; Altmann et



65 al., 2020; Cody et al., 2020; Betz-Nutz, 2021; Zhong et al., 2022). These erosion processes are primarily driven by temperature
66 and precipitation events, which have been subject to change in recent years and decades (Serquet et al., 2011; Brugnara et al.,
67 2012; Mankin and Diffenbaugh, 2015; Klein et al., 2016; Beniston et al., 2018; Hock et al., 2019; IPCC, 2021; Pepin et al.,
68 2022). Spring-time snowmelt provide important preparatory steps for sediment transport processes, such as loosening of the
69 upper layers of sediments of the slope or through the delivery of material into the gullies by nival processes, which is then
70 transported downslope by debris flows in the summer months (Haas et al., 2012; Dusik et al., 2019), which is considered as
71 the most important process occurring (Ballantyne, 2002a; Curry et al., 2006). Dusik (2019) also shows a positive correlation
72 between the number of mass movements and the number of extreme precipitation intensities, the number of certain threshold
73 exceedances for extreme daily precipitation totals as well as annual precipitation totals. These processes ultimately lead to the
74 dissection of the upper parts of the lateral moraines which is, however, limited in time (Curry et al., 2006). Curry et al. (2009)
75 inferred from morphometric measurements along a chronosequence that gullies increase in depth, width, area, and volume
76 over time, with width increasing significantly more than depth, resulting in the older ones not being as densely gullied.
77 Furthermore, it is described that the slope gradient decreases over time, e.g. Ballantyne and Benn (1994) report an average of
78 5° (in 48 years between 1943 and 1991). Betz-Nutz et al. (2022) document a range of slope gradient changes between -3.2°
79 and $+6.6^\circ$ between the ~1950s and 2018 (~68 years), showing that both increases and decreases can occur. Ballantyne and
80 Benn (1994), Curry (1999) and Curry et al. (2006) give average annual erosion rates of different gully systems over several
81 decades estimated by the volume of the gullies. Curry et al. (2006) showed at different test sites in the Swiss Alps that the
82 maximum extent of gullies is reached after 50 years of ice release and that sediment filling and stabilisation occurs after 80-
83 140 years of deglaciation. While 50% of the available sediment is exhausted after 10-50 years, it can take several centuries
84 until the paraglacial adjustment process is completed (Curry et al., 2006). Schiefer and Gilbert (2007) show, based on
85 quantitative analyses (via stereo-photogrammetry using historical aerial images), a significant decrease in the geomorphic
86 activity of gully systems on lateral moraines over several decades and different epochs in the glacier forefield of the Lillooet
87 Glacier (Canada, British Columbia). Carrivick et al. (2013) generally confirm the concept of paraglacial adjustment by showing
88 decreasing morphodynamics with increasing distance from the glacier as they have been ice-free for a longer time. However,
89 the lower morphodynamics observed in the distal areas of the glacier forefields could also be due to the generally lower slope
90 gradients there (Betz-Nutz et al., 2022). Lane et al. (2017) showed in the glacier forefield of Haut Glacier d'Arolla (Switzerland,
91 Valais) that there are no indications of filling in the developed gully systems, which indicates that they are still in the incision
92 phase. Betz-Nutz et al. (2022) show with the use of historical aerial photographs (processed by SfM-photogrammetry) that the
93 paraglacial adjustment process over decades is very variable. While 13 out of 20 moraine sections showed decreasing erosion
94 rates over decades, divided into several epochs, six showed almost constant activity and one section even showed a substantial
95 increase in erosion rate.

96 The period of paraglacial landscape adjustment is also influenced by upcoming vegetation, which can be considered both a
97 consequence and a cause of slope stabilisation (Eichel et al., 2016; Haselberger et al., 2021; Haselberger et al., 2022).



98 Nevertheless, bound solifluction processes can occur under a dense vegetation cover and are therefore not an absolute sign of
99 stabilisation (Draebing and Eichel, 2017).

100 The generation of multitemporal accurate and precise digital elevation models (DEMs) and the resulting DEM of Differences
101 (DoDs) by different remote sensing methods and techniques, which have been established in geomorphological research in
102 recent years, enabled the detection of changes in the Earth's surface in high spatial and temporal resolution (Pulighe and Fava,
103 2013; Nebiker et al., 2014; Tarolli, 2014; Smith et al., 2016; Eltner et al., 2016; Sevara et al., 2018; Okay et al., 2019). By
104 processing overlapping high-resolution digitised historical aerial images (HAI) of high alpine geosystems, using SfM-MVS
105 (Structure-from Motion with Multi-View-Stereo) digital stereo-photogrammetry in combination with current airborne LiDAR
106 (Light Detection And Ranging) data into DEMs and the corresponding DoDs, landscape changes in these areas can be
107 reconstructed over several decades (Midgley and Tonkin, 2017; Mölg and Bolch, 2017; Lane et al., 2017; Betz et al., 2019;
108 Altmann et al., 2020; Fleischer et al., 2021; Betz-Nutz, 2021; Stark et al., 2022; Piermattei et al., 2022). The spatial distribution
109 of positive and negative DoD elevation changes enable various analyses, such as the reconstruction and interpretation of
110 individual geomorphological processes (Dusik, 2019) or the calculation of morphological budgets (Altmann et al., 2020).

111 Furthermore, by applying flow routing algorithms and the accumulation of DoD values accordingly, sediment yield (SY) from
112 the contributing area of each cell can be determined: Pelletier and Orem (2014) used repeat airborne LiDAR-based DEMs
113 before and after a wildfire and calculated for each pixel the net sediment volume exported by geomorphological processes.
114 Further applications of this methodology have been published by Wester et al. (2014), who calculated the total SY by applying
115 a weighted flow accumulation algorithm, and Heckmann and Vericat (2018), who further developed the approach by
116 calculating a spatially distributed measure of functional sediment connectivity on a proglacial slope. Neugirg et al. (2015a;
117 2015b; 2016) showed a positive correlation between log SY (calculated by accumulated DoD values on slopes) and the
118 corresponding log SCA (sediment contributing area), respectively log CA (catchment area), both extracted at randomly
119 selected cells of the channel network (so-called "virtual sediment traps", VST). Besides to these studies, which were carried
120 out on hillslopes in the Northern Alps (Germany, Lainbach valley and Arzbach valley) and at a former iron ore mine on the
121 island of Elba in the Tyrrhenian Sea (Italy, next to Rio Marina)), this approach was also applied to one proglacial slope in the
122 Kaunertal (Austria, Tyrol) by Dusik (2019) and Dusik et al. (2019). One advantage of this approach is that it can be used to
123 determine not only the size of SY (which can be compared with previous epochs, for example), but also the variability of SY
124 in the AOI within an epoch (spatial pattern of SY within the AOI), which is not possible, for example, when calculating simple
125 erosion rates, where only the volume of the total change can be computed.

126 In order to better understand the paraglacial adjustment process of lateral moraines, we continue the application of the approach
127 of Neugirg et al. (2015a; 2015b; 2016), Dusik (2019) and Dusik et al. (2019) to different LIA lateral moraines in the central
128 Eastern Alps in this study, which has so far only been carried out on one proglacial slope and over a short epoch of a few
129 months (Dusik et al., 2019). Secondly, we show volume calculations of the entire AOIs to determine the total sediment yield
130 (and erosion rates). Combining high-resolution historical and current DEMs and the corresponding DoDs, we show, the
131 quantification and analysis of gully system morphodynamics at 12 different sections in the upper reaches of lateral moraines



132 in five different glacier forefields over a total epoch of several decades (1953-2019) with several survey periods (~1950s to
 133 ~1970s, ~1970s to ~2000s and ~2000s to 2017/2019). By using simulated climate data of the glacier forefields we were able
 134 to investigate, besides system-internal influences, also external impacts on the morphodynamics, which have not been
 135 considered in long-term studies on erosion of LIA lateral moraines so far.

136 2 Study Area

137 The areas of interest (AOIs) are located in different high alpine geosystems along a north-south axis in the central Eastern Alps
 138 and are situated north (Horlachtal and upper Kaunertal) and south (upper Martelltal) of the main alpine divide. In these valleys,
 139 the AOIs are located within five glacier forefields on lateral moraines formed by the glaciers during their maximum glacier
 140 extent during the LIA around 1850 (Figure 1). The Horlachtal is located in the Stubai Alps (Tyrol, Austria), which is a tributary
 141 of the Oetztal (Geitner, 1999; Rieger, 1999). The investigated section of the Horlachtal is located in the side valley and sub-
 142 catchment Grastal (glacier forefield Grastalferner), which is oriented in a north-south direction. Geologically, the Horlachtal
 143 is located in the Oetztal Massif, where gneisses and mica schists dominate (Becht, 1995; Geitner, 1999). The Kaunertal is also
 144 located in the Oetztal Alps (Tyrol, Austria) and is oriented in a north-south direction. This valley geologically belongs to the
 145 Austroalpine crystalline complex (Tollmann, 1977; Geological Survey of Austria, 1999) where crystalline rocks, mainly ortho-
 146 and paragneisses, dominate (Vehling, 2016). The AOIs within the Kaunertal are located in the glacier forefields of the
 147 Gepatschferner, another glacier outlet of the Gepatschferner, the so-called Münchner Abfahrt (MA), and the Weißseeferner.
 148 The Martelltal is a southwest-northeast oriented valley located in the Ortler-Cevedale group (South Tyrol, Italy) and belongs
 149 geologically to the Ortler-Campo Crystalline, where quartz phyllite dominates with layers of e.g. shales, gneisses and marbles
 150 (Mair and Purtscheller, 1996; Staindl, 2000; Mair et al., 2007). The two AOIs are located in the glacier forefield of the
 151 Hohenferner. All valleys are characterized by the continental climate and low annual precipitation sums of the inner alpine dry
 152 region (Becht, 1995; Hagg and Becht, 2000; Veit, 2002; Hilger, 2017; Betz-Nutz, 2021). The AOIs are characterized by very
 153 low vegetation cover, intense paraglacial morphodynamics and typical unsorted moraine material. Table 1 and Figure 1 give
 154 an overview of the location as well as the characteristics of the AOIs.

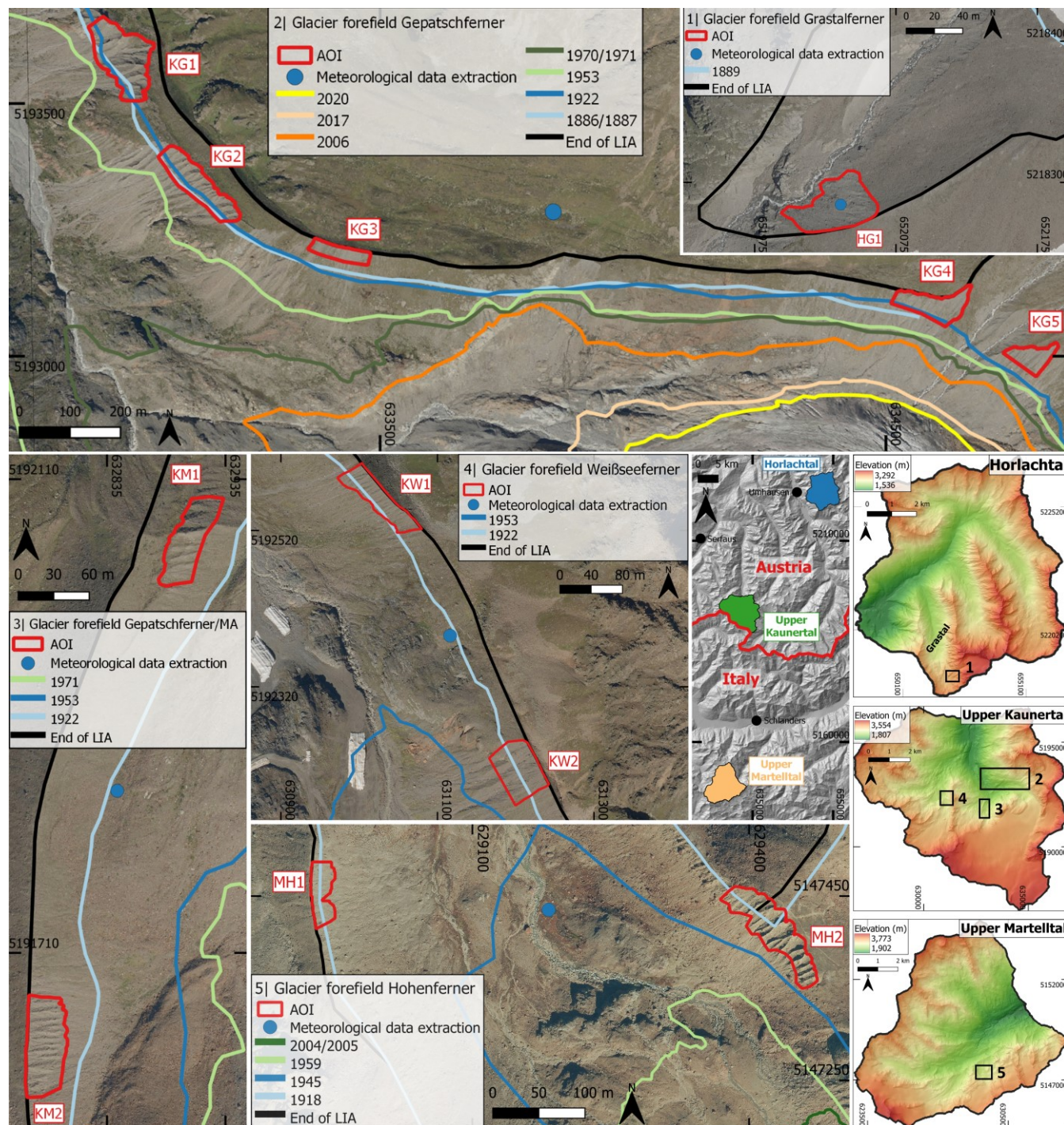
155 **Table 1: Characteristics of the AOIs. Values were derived from 2017 DEM (Kaunertal) and 2019 DEM (Horlachtal and Martelltal).**

AOI	Location (Centre) (ETRS89/ UTM Zone 32N, EPSG Code: 25832)	Elevation (Ellipsoidal heights) (m)	Aspect	Size (m ²)	Max. length of delineated AOI (downslope) (m)	Mean (and max.) slope gradient (°)	At least ice- free since (years)*	Glacial or dead ice influence at the foot of the slope
HG1	E 652032, N 5218283	2659-2696	W	1647	43	37.9 (46.8)	1860 (159)	Not detectable
KG1	E 632991, N 5193590	2183-2262	W	12431	124	41.5 (69.3)	1937 (80)	Not detectable
KG2	E 633140, N 5193339	2244-2321	SW	8814	59	43.8 (61)	1933 (84)	Until 2006
KG3	E 633421, N 5193204	2329-2400	S	3123	29	38.5 (48.3)	1872 (145)	Not detectable
KG4	E 634596, N 5193101	2540-2620	SW	6193	99	41.1 (61.3)	1929 (88)	until today



KG5	E 634789, N 5192997	2580-2645	SW	3531	77	44.3 (57.1)	1913 (104)	until today
KM1	E 632904, N 5192058	2443-2486	E	2025	23	39.8 (46.9)	1903 (114)	Not detectable
KM2	E 632783, N 5191632	2560-2598	E	2534	30	45.7 (56.7)	1901 (116)	Until 2006
KW1	E 631025, N 5192561	2546-2603	SW	2951	38	41.6 (54.4)	1924 (93)	Not detectable
KW2	E 631204, N 5192213	2682-2714	SW	3638	49	39.9 (53.4)	1937 (80)	Until 2006
MH1	E 628937, N 5147454	2704-2729	E	1475	26	35.5 (51.6)	1921 (98)	Not detectable
MH2	E 629426, N 5147413	2755-2796	SW	3983	45	45.3 (72)	1943 (76)	Until 2004/2005

156 *Determination of complete deglaciation is based on an interpolation between the two glacier extensions within which the AOIs have become ice-
157 free by calculating the euclidean distance as proposed by Betz-Nutz et al. (2022).



158

159 **Figure 1:** Location of AOIs, glacier extents (Sources in Table 2) and location for meteorological data extraction (for corresponding
 160 analysis, see sec. 3.3). Large-scale elevation data (DSM, 25 m) (centre right) are based on SRTM and ASTER GDEM (Copernicus,
 161 2016). DEMs (1 m) (right and bottom right) are based on airborne LiDAR (ALS) data from 2017 (Kaunertal) and 2019 (Horlachtal
 162 and Martelltal) (see sect. 3.1.1). Orthophotos (from 2020) are provided by the Province of Tyrol (Horlachtal and Kaunertal) and by



163 the Autonomous Province of Bolzano, South Tyrol (Martelltal). The glacier extent of Groß and Patzelt (2015) is based on mapping
 164 of the LIA lateral moraines and field surveys based on orthophotos. In the process of this study, these mappings were slightly
 165 modified so that they fit to the maximum glacier extent (LIA lateral moraines) more accurately. The glacier extents end of LIA,
 166 1918, 1945 and 1959 in the Martelltal have already been described by Betz et al. (2019).

167 **Table 2: Sources of the glacier extents.**

Valley	Year	Source
Horlachtal	End of LIA	Groß and Patzelt (2015)
	1889	Gedächtnisspeicher Ötztal (Austria, Längenfeld), K&K Militärgeographisches Institutsarchiv*
Kaunertal	End of LIA	Groß and Patzelt (2015)
	1886/1887	Finsterwalder and Schunck (1888)*
	1922	Finsterwalder (1928)*
	1953	Images of BEV, DoD 1953/2017***
	1970/1971	Images of the Office of the Tyrolean Government, DoD 1970/1971-2017***
	2006	Province of Tyrol, DoD 2006-2017***
Martelltal	2017	Chair of Physical Geography, Cath. University Eichstätt-Ingolstadt, SEHAG-project (See sect. 3) **
	2020	Province of Tyrol, orthofoto**
	End of LIA	Mapped on base of visible moraines and descriptions of Finsterwalder (1890)
	1918	Spezialkarte 1:75.000 of BEV*
	1945	Images of the IGMI, orthofoto*
	1959	Images of IGMI, DoD 1959-2019***
	2004/2005	Autonomous Province of Bolzano, DoD 2004/2005-2019***

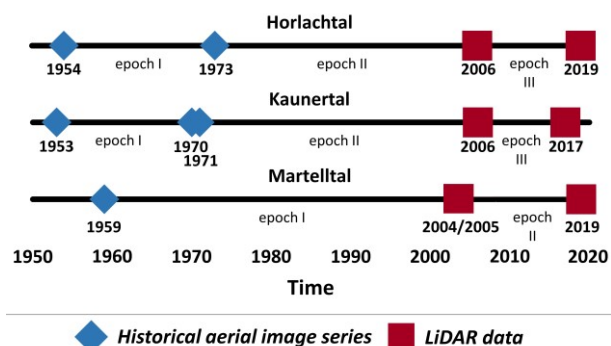
168 *based on historical map, **based on orthophoto and/or hillshade and ***based on DoD (SfM-MVS/photogrammetry and/or ALS).

169 3 Material and Methods

170 3.1 Generation of the topographic data

171 3.1.1 Processing of airborne LiDAR and photogrammetric/SfM-MVS point clouds

172 Several data sets were used for the reconstruction of the terrain surface for the entire catchments. These include both current
 173 airborne LiDAR data and historical aerial image series (Figure 2). Thus, the epochs are based on the availability and quality
 174 of the data.



175

176 **Figure 2: Data and epochs.**

177 To determine the recent morphodynamics in the respective AOIs, available airborne LiDAR data from 2004/2005 to 2019
 178 were used. The 2004/2005 and 2006 data of the three valleys were provided by the Autonomous Province of Bolzano and the
 179 Province of Tyrol (Table 3). The latest ALS datasets of each valley (2017 and 2019) were collected in own ALS flight
 180 campaigns of the Chair of Physical Geography at the Catholic University of Eichstätt-Ingolstadt (Table 3) (Stark et al., 2022).
 181 In this case, LiDAR data sets were collected using previously determined flight strips. Direct georeferencing (position and
 182 altitude) of the trajectories was determined by Global Navigation Satellite System (GNSS) rover antenna and an Inertial
 183 Measurement Unit (IMU) (Applanix AP 20), both located in the laser scanner. In addition, GNSS correction data were acquired
 184 on the ground during the flight missions using a dGNSS antenna (Figure 3). Subsequently, the GNSS/IMU trajectory data
 185 were processed in three steps. This included, (i) the calculation of precise trajectories using the software PosPac MMS
 186 (Applanix), (ii) the attachment of raw scans to the flight lines using the software package Riegl RiProcess, and finally (iii) a
 187 strip adjustment in the processing software OPALS (Pfeifer et al., 2014) using the approach of Glira et al. (2015).

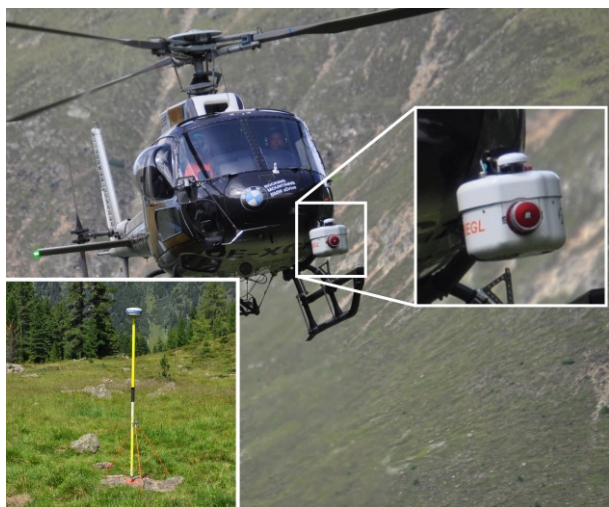
188 **Table 3: Overview of the ALS (and DEM) data.**

Valley	Date of acquisition	Source/Purpose	Laser-scanner	Field of view (°)	Flying altitude (metre above ground)	Air-speed (kn)	Laser pulse Measuring frequency (khz)	Wave-length (nm)	DEM res. or mean point density of the AOIs (points/m ²)
Horlachtal	05.09.2006	Province of Tyrol	N/A	N/A	N/A	N/A	N/A	N/A	DEM, 1 m
	08.08.2019	SEHAG project (“SEnsitivity of High Alpine Geosystems to climate change since 1850”)	Mobile laser scanner VPI (Riegl VuxSys-LR)	180	~150	~45	200	1550	24.1
Kaunertal	05.09.2006	Province of Tyrol	N/A	N/A	N/A	N/A	N/A	999	3.4
	05.07.2017	PROSA project (“High-resolution measurements of morphodynamics in rapidly changing	Mobile laser scanner VPI (Riegl	180	~150	~45	200	1550	35.7



Martelltal	2004/2005	PROglacial Systems of the Alps") Autonomous province of Bolzano	VuxSys-LR)	N/A	N/A	N/A	N/A	N/A	1.4
	09.08.2019	SEHAG project ("SEnsitivity of High Alpine Geosystems to climate change since 1850")	Mobile laser scanner VPI (Riegl VuxSys-LR)	180	~150	~45	200	1550	13.3

189



190

191 **Figure 3: ALS data collection on 08.08.2019 in Horlachtal. Helicopter with nose-mounted VPI laser scanner as well as the ground**
 192 **station which recorded the dGNSS raw data during the flight time (Stonex S9III).**

193 In order to extend the temporal scope of this study by several decades (until 1953), previously digitised (high-resolution)
 194 overlapping HAI were processed into historical DEMs. Except for the 1959 Martelltal-survey, camera distortion parameters
 195 and focal lengths were provided for all data with the respective camera calibration certificates (Table 4).

196 The digitised image series were processed with the Agisoft Metashape Professional software package (Version 1.6.6; Agisoft
 197 LLC) using Structure from Motion (SfM) photogrammetry with multi-view-stereo (MVS) algorithms to generate high-
 198 resolution point clouds. The generation of point clouds from digitised historical (aerial)image series requires different
 199 preparation and processing steps. First, all images of each series were resized to a common image size (uniform number of
 200 pixels along the x- and y-axis) without changing the image content. This step was necessary so that the software can assign all
 201 images to the same camera (source) and was carried out using Adobe Photoshop (CS6). This is of enormous importance in
 202 order to be able to use the appropriate distortion parameters for the respective camera models for the calculation. After, the
 203 image sets were imported into single folders and a common global coordinate system (ETRS89/UTM zone 32N; EPSG code:
 204 25832) was defined. Next, all images were masked to exclude the black borders/frame (instrument stripes with the camera
 205 metadata) in order to avoid interference with the orientation of the cameras (Gomez et al., 2015). Before the initial processing



206 of images we defined the fiducial mark information and lens distortion parameters in order to set the metric dimension of
 207 images and lenses. This informations were included and used for the alignment of single images (SfM).
 208 Since a global exterior orientation requires a large number of precisely surveyed ground control points (GCPs) distributed
 209 throughout the area, we used highly-precise ALS datasets with millimetre accuracy (2019 Horlachtal; 2017 Kaunertal) to
 210 extract these GCPs and to define the exterior orientation of all data. The selection and extraction of GCPs was based on clearly
 211 identifiable objects (e.g. rock formations) that were also considered as stable (geomorphologically unchanged) over the entire
 212 observation period. If a calibration certificate was available, the film camera option was used, fiducial marks defined, the focal
 213 length set and fixed. All other lens distortion parameters ($C_x, C_y, k_1, k_2, k_3, p_1$ & p_2) were estimated and adjusted fully automatic
 214 using the auto-calibration function. In case of missing camera calibration certificate, an auto-calibration (no film camera) was
 215 performed. Both options were proposed by Stark et al. (2022).
 216 According to these pre-processing steps, the point clouds were generated by (i) initial joint orientation of the images, (ii)
 217 selection of ground control points (GCPs), (iii) final camera orientation (bundle block adjustment) including scale definition,
 218 and (iv) calculation of dense point clouds.

219 The processing of the 1959 point cloud, which was used in this study, is already described in Betz et al. (2019).

220 **Table 4: Overview of acquired historical image series for point cloud generation and corresponding DEMs by photogrammetry/SfM.**

	1953 (Kaunertal)	1954 (Horlachtal)	1959 (Martelltal)	1970 (Kaunertal)	1971 (Kaunertal)	1973 (Horlachtal)
Source/ Purpose	BEV/Forest condition estimation; Flight C	BEV/Forest condition estimation; Flight D	IGMI	Office of the Tyrolean Government/ Tyrolean state Surveying flight	Office of the Tyrolean Government/ Tyrolean state Surveying flight	Office of the Tyrolean Government/ Tyrolean state Surveying flight
Date of acquisition	31.08.1953/ 01.09.1953/ 08.09.1953	31.08.1954/ 04.09.1954	09.09.1959/ 20.09.1959	29.09.1970	18.08.1971	06.08.1973
Flying altitude (m a.s.l)	ca. 5955/ unknown ca. 5850	ca. 6110/ ca. 5920	ca. 5100/ ca. 5000	ca. 8665	ca. 5025	ca. 4900
Camera	Wild RC/5	Wild RC/5	Santoni	Wild RC5/RC8	Wild RC5/RC8	Wild RC5/RC8
Number of images	36/51/63	32/4	2/6	26	31	88
Focal length (mm)	210.11	210.23	153.41	210.43	209.48	210.43
Scanning Resolution (μ m)	15	15	N/A	12	12	12
Format	TIFF	TIFF	TIFF	TIFF	TIFF	TIFF
Calibration protocol available	yes	yes	no	yes	yes	yes
Number of GCPs	100	74	23	88	29	67



Mean point density (points/m ²)*	8.5	3.7	4.9	13.3	15.7	20.5
Ground resolution (cm/pix) **	22.5	34.8	19.6	19	17	13.8
RMS reprojection error (pix) **	0.48	0.51	1.55	0.86	0.44	0.45

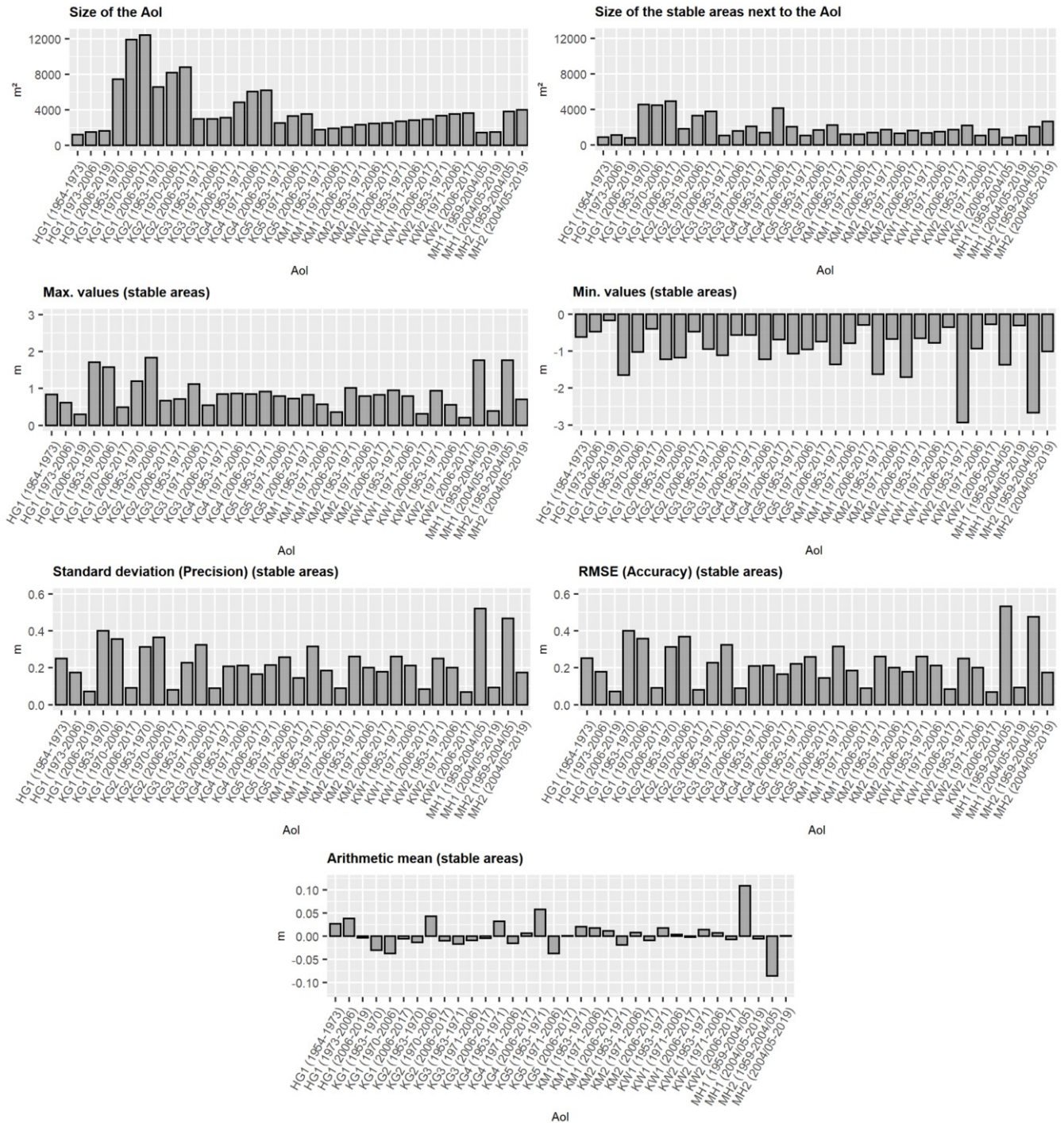
221 *refers to the exact AOIs, **refers to the entire data set

222 3.1.2 Digital elevation model (DEM) and DEM of Difference (DoD) processing

223 Although all point clouds were finally available in the same coordinate system (ETRS89/UTM Zone 32N, EPSG Code: 25832), a
 224 local adjustment of each AOI was carried out to obtain the highest possible accuracy of the subsequent DoDs to be calculated.
 225 For this purpose, stable areas, i.e. geomorphologically unchanged areas such as rock outcrops or stable areas on the lateral
 226 moraines, were mapped next to each AOI based on orthophotos. To match the point clouds as well as possible, the Iterative
 227 Closest Point algorithm (ICP) (Besl and McKay, 1992; Bakker and Lane, 2017) implemented in SAGA-LIS (Conrad et al.,
 228 2015) was used for fine registration. Previously, the LiDAR based point clouds were further processed in the software SAGA-
 229 LIS (LIS Pro 3D) from Laserdata (laserdata.at) in combination with Python and R to prepare point clouds for the generation
 230 of high-resolution digital elevation models (DEMs). This included the removal of outliers (Remove Isolated Points), a ground
 231 classification (to remove vegetation), which was carried out with a modified approach according to Hilger (2017) and the
 232 achievement of more homogeneous point clouds with the tool 3D Block Thinning (PC) in SAGA-LIS. The point clouds were
 233 then converted into DEMs using the Point Cloud to Grid tool in SAGA-LIS (elevations of points averaged for each raster cell;
 234 cell sizes for Horlachtal and Kaunertal 1m, for Martelltal 2m). Finally, the DoDs were generated by subtracting the individual
 235 DEMs from each other to determine the positive and negative elevation changes of the earth's surface.

236 3.1.3 Uncertainty assessment

237 The presence of various uncertainties in differently generated DEMs (Hodgson and Bresnahan, 2004; Bakker and Lane, 2017)
 238 also leads to uncertainties in the resulting DoDs (Lane et al., 2003; Rolstad et al., 2009; Cavalli et al., 2017; Anderson, 2019).
 239 Therefore, an uncertainty assessment was carried out using the DoD values from stable areas near each AOI. The size of the
 240 stable areas varied between 25% and 75% of the size of the corresponding AOI. In addition to the estimation of the precision
 241 (Std Dev) and accuracy (RMSE), the arithmetic mean, minimum and maximum values were also determined (Figure 4).



242

243 Figure 4: Uncertainty assessment.



244 To determine the uncertainty of the sediment volume change (total sediment output, Figure 7), the error propagation method
245 for uncorrelated, correlated and systematic error according to Anderson (2019) was applied. We chose not to threshold our
246 DoDs by a Level of Detection following Anderson's (2019) clear recommendation not to apply thresholding to net volumetric
247 change analysis where thresholding can lead to biased results.

248 For the final determination of the total error, the following formula was applied Eq. (1):

$$249 \sigma_v = \sqrt{\sigma_{v,re}^2 + \sigma_{v,sc}^2 + \sigma_{v,sys}^2} \quad (1)$$

250 where $\sigma_{v,re}$ is the uncorrelated error, $\sigma_{v,sc}$ spatially correlated error and $\sigma_{v,sys}$ systematic error.

251 3.2 Derivation of the regression lines

252 In this study, we followed the SCA approach of Neugirg et al. (2015a; 2015b; 2016) and Dusik et al. (2019), who applied this
253 approach at the slope scale and replaced real sediment traps in the channels, as originally based on the work of Haas (2008)
254 and Haas et al. (2011), with so-called virtual sediment traps (VSTs) in modelled channels in a DEM. The SCA model represents
255 a set of simple DEM-based rules according to Heinimann et al. (1998) for delineating those geomorphologically active areas
256 that potentially deliver sediment to the channel network (and hence constitute the sediment contributing area of the latter).
257 This approach is similar to the "effective catchment area" proposed by Fryirs et al. (2007) and Fryirs (2013). By selecting
258 different parameters related to topography and landcover information, namely the minimum channel gradient threshold (for
259 longitudinal (de-)coupling), the minimum slope gradient threshold (for lateral (de-)coupling), the maximum distance from
260 channel (slope length) and a weighting of the vegetation cover (representing the role impedance of vegetation as a disturbing
261 factor into sediment transport), Haas (2008) and Haas et al. (2011) reduced the hydrological catchment accordingly to the
262 sediment supplying and thus the sediment contributing area (SCA). A correlation between the size of the SCA, which thus
263 corresponds to a subset of the hydrological catchment, and the computed sediment yield (determined by sediment traps in the
264 channels) could be shown, but no correlation between the size of the hydrological catchment and the sediment yield. This
265 shows that only a certain part within a hydrological catchment is geomorphologically active, providing sediment to the
266 channels and subsequently transporting it downstream, as covered areas and areas with low gradients (hillslope and channel
267 sections) reduce sediment connectivity within a catchment. Linear regression analysis was used to show this significant
268 correlation, which is formulated as Eq. (2):

$$269 y = \text{intercept} + \text{slope} * x, \quad (2)$$

270 where y is (log.) mean annual bedload sediment yield and x (log.) SCA.

271 The SCA model uses an empirical relationship between log. sediment contributing area as the independent variable and log.
272 mean annual bedload sediment yield as the dependent variable. Thus, the SCA can be used as a predictor of sediment delivery
273 in alpine catchments. This has already been confirmed in several studies in both small and large catchments (ranging from



274 hectare to square kilometres) and in different regions such as the Northern Calcareous Alps (Haas, 2008; Haas et al., 2011;
275 Sass et al., 2012; Huber et al., 2015) and the French Northern Alps/Prealps (Altmann et al., 2021).

276 Finally it can be stated that a linear dependency of two variables x and y on a log-log-scale has a fundamentally different
277 behavior than a usual linear dependency. In our case, we have $y = \log(\text{SY})$ and $x = \log(\text{SCA})$. Back-transformation of Eq. (2)
278 using the *exp* function yields gives the following relation between SCA and SY, Eq. (3):

$$279 \text{SY} = \exp(\text{intercept}) * \text{SCA}^{\text{slope}} \quad (3)$$

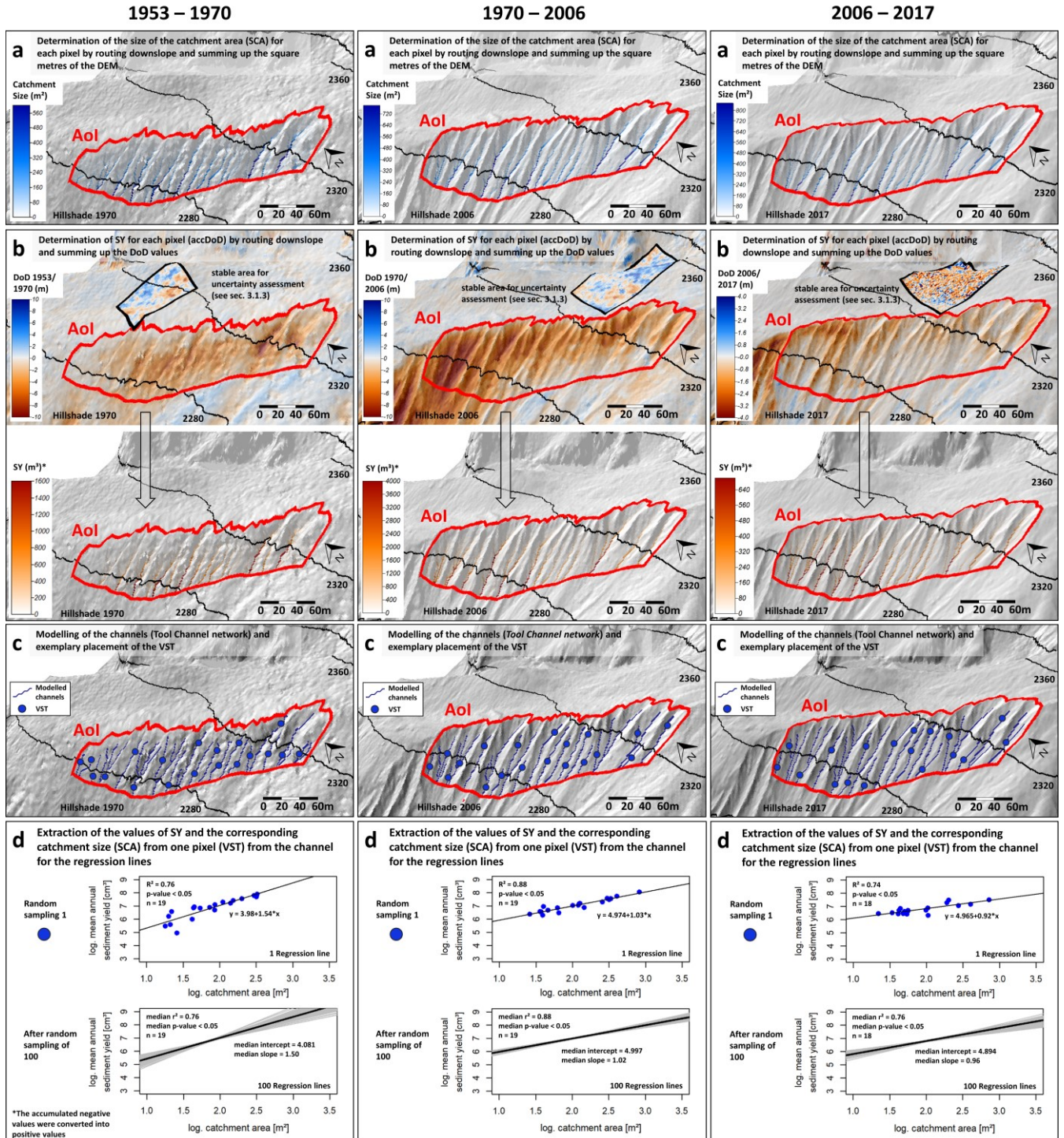
280 Thus, the relation between SY and SCA is a polynomial of the form $y = a * x^b$. In particular, the slope in the log-log model
281 represents the exponent of the polynomial in the standard model. The relation between SY and SCA is (nearly) linear if slope
282 is (close to) one. In this case, the exponential of the intercept in the log-log model represents the slope of the linear relation in
283 the standard model, meaning that independent of the actual size of the SCA, one square meter provides the same amount of
284 SY, given by *exp(intercept)*. On the other hand, if the slope in the log-log model is considerably greater than one, the
285 standard model shows a polynomial behaviour, meaning that in the same AOI, increasing the SCA provides more SY per
286 square meter.

287 The steps of the SCA approach of this study are composed as follows and were implemented in SAGA LIS and R. The elevation
288 changes in DoDs (using no threshold) generated from multitemporal data were routed downslope and accumulated using the
289 D8 algorithm (O'Callaghan and Mark, 1984). The resulting accumulated DoD values (accDoD) in every raster cell corresponds
290 to the net volume of the sediment balance within its contributing area. On steep slopes, accDoD will be negative and represents
291 the sediment yield of this contributing area (Pelletier and Orem, 2014); if it is close to zero, it means that all eroded sediment
292 has been re-deposited within the contributing area. As in the previous SCA studies by Neugirg et al. (2015a; 2015b; 2016), the
293 application of the parameters used in the original SCA model (Haas, 2008; Haas et al., 2011), which lead to the reduction of
294 the hydrological catchment to the SCA, is omitted because the AOIs and the modelled channels are consistently steep,
295 uncovered and have short slope lengths, which makes this reduction obsolete. Therefore, the SCA is identical to the catchment
296 area (CA) in this study.

297 In detail, channel initiation points were delineated using a threshold of 20 m² of the flow accumulation that was computed
298 using the D8 algorithm (O'Callaghan and Mark, 1984). Channels that were shorter than 10 m were discarded. To ensure
299 statistical independence through avoiding overlapping contributing areas, a stratified sampling scheme was adopted that
300 included one randomly selected raster cell per channel. Pairs of values (SY and the corresponding SCA size) were randomly
301 extracted from the corresponding channels (representing the VSTs) for each AOI and a regression line were calculated
302 accordingly. To quantify the uncertainty due to random selection, this sample was repeated 100 times, resulting in 100
303 regression models of SY on SCA.

304 Furthermore, we added two conditions and further developed the SCA approach accordingly. In order to obtain more stable
305 regression lines, the range of values of the SCA size was divided into quartiles (with equal number of cells within the quartiles)
306 to ensure a homogeneous distribution of the extracted values. Additionally samples that contained points with a high leverage

307 (greater than 0.5) in the regression model were discarded, and the sampling was repeated until a number of 100 samples was
 308 reached.



309



310 **Figure 5: Example derivation of the statistical relationship at AOI KG2.**

311 **3.3 Calculation of the sediment output**

312 Additionally, the total sediment output volume, the mean annual sediment output (divided by the corresponding number of
313 years) and the specific mean annual sediment output (additionally divided by the area of the AOI) were calculated for each
314 AOI and epoch.

315 The following equation was used for this (4):

$$316 V = \sum D oD * L^2, \quad (4)$$

317 where $\sum D oD$ is the sum of the corresponding DoD subset values and L^2 is the cell size.

318 **3.4 Generation of meteorological data**

319 Using data generated with a regional climate model (RCM), the influence of the changes in climate forcing (air temperature
320 and precipitation) on morphodynamics was investigated. For dynamical downscaling of climate data for the beginning of the
321 study period until 2015, we used the Advanced Research Version of the Weather Research and Forecasting (ARW-WRF)
322 model (version 4.3), which is based on fully compressible and non-hydrostatic equations (Skamarock and Klemp, 2008). The
323 20th Century Reanalysis version 3 (20CRv3) dataset (Compo et al., 2011; Giese et al., 2016; Slivinski et al., 2019), with a
324 spatial and temporal resolution of $1^\circ \times 1^\circ$ and three hours, respectively, was used as driving data (initial and boundary
325 conditions). The simulation was performed in three nested domains with grid spacing of 18- (Domain 1), 6- (Domain 2), and
326 2-km (Domain 3). For our simulations, we mainly used the physics and dynamics options proposed by Collier and Mölg
327 (2020), and are listed in Table 5. However, the Noah land surface model, prescribed eta levels by Collier et al. (2019), and the
328 24 United States Geological Survey (USGS) land use categories were used. The temporal resolution of simulated data in D3
329 is 1 hour for temperature and 15 minutes for precipitation.

330 **Table 5: Overview of the WRF configuration.**

Domain configuration	
Horizontal grid spacing	18-, 6-, 2-km (D1, D2 and D3)
Grid dimensions	190 x 190, 151 x 142, 121 x 139
Lateral boundary condition	variable (20CRv3 at $1^\circ \times 1^\circ$, 3-hour)
Time step	90, 30, 10 s
Vertical levels	50
Model top pressure	10hPa
Model physics	
Microphysics	Morrison (Morrison et al., 2009)
Cumulus	Kain-Fritsch (none in D3) (Kain, 2004)
Radiation	RRTMG (Iacono et al., 2008)



Planetary boundary layer	Yonsei State University (Hong et al., 2006)
Atmospheric surface layer	Monin Obukhov (Jiménez et al., 2012)
Land surface	Noah (Chen and Dudhia, 2001)

Dynamics

Top boundary conditions	Rayleigh damping
Diffusion	Calculated in physical space

331

332 For the period from 2016 to the end of the study period (2017/2019), the ERA5 reanalysis dataset (Hersbach et al., 2018) was
333 used (spatial resolution: 55 km, temporal resolution: 1 hour). The different meteorological datasets were combined and divided
334 into the corresponding study epochs. For this purpose the temporal resolution of the precipitation data simulated with WRF
335 was adjusted to one hour to fit the ERA5 temporal resolution. The simulated temperature and precipitation data were extracted
336 at the location of each of the five glacier forefield (Figure 1). These are the centres of the respective AOIs and represent the
337 corresponding glacier forefield. In addition, a corresponding elevation correction of the climate data was applied for
338 temperature.

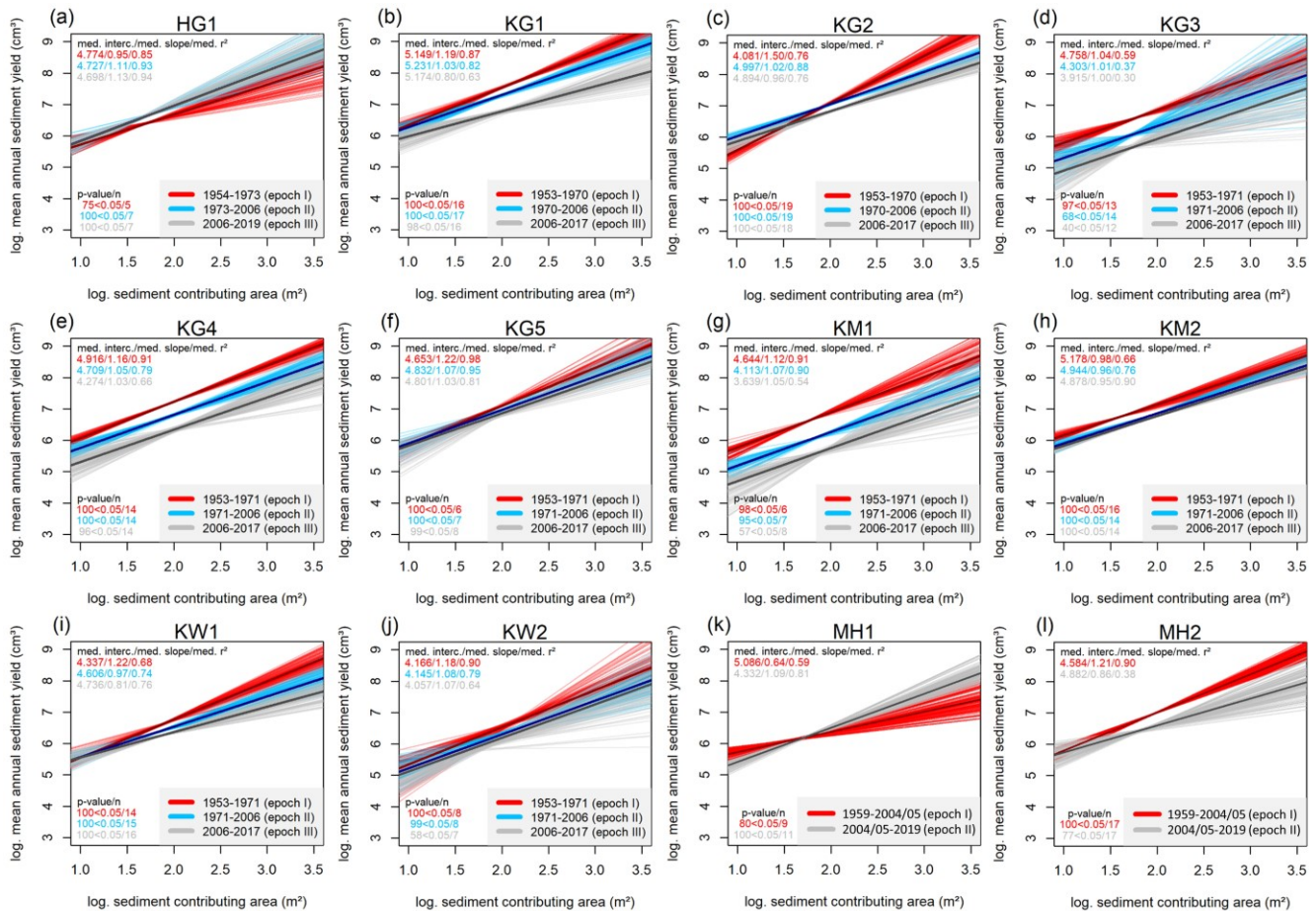
339 For the analysis, we used the mean annual air temperature (2 metres above ground), as well as the corresponding trends and
340 the mean number of ice days (days with maximum temperature $<0^{\circ}\text{C}$). In addition, the number of warm air inflows from
341 October to May was determined in order to identify corresponding snowmelt processes on the AOIs. A warm air inflow is
342 defined as a period of at least 3 days in which more than 70% is above 0°C , following a previously colder period of 5 days
343 (100% below 0°C). In addition, the precipitation patterns were analysed. For this purpose, the mean annual precipitation totals,
344 the mean annual winter (October to May) and the mean annual summer precipitation totals (June to September) as well as the
345 corresponding trends were determined in order to identify seasonal changes. Furthermore, various continuing classes (4 mm
346 for one-hour resolution and 10 mm classes for daily totals) were used to analyse corresponding changes in individual extreme
347 events and daily precipitation totals. Individual precipitation events were defined as one event, regardless of length, if they
348 were contiguous throughout, and were separated if there was no precipitation for at least one hour. To minimise the noise
349 generated in the data, both datasets were also filtered for extremely small events by changing the values from <0.01 mm to 0
350 mm. The calculation of the mean annual winter precipitation was always carried out over the entire winter. For example, for
351 the winter of 1953, data from October 1952 to May 1953 was included. The average summer precipitation was calculated
352 accordingly from June 1953 to September 1953. Furthermore, precipitation was differentiated into snow and rain events. The
353 determination of a threshold to distinguish rain from snowfall is very dynamic in mountainous regions and difficult to estimate.
354 However, the difference between rain to snow depends mainly on surface air temperature as well as air humidity, with snow
355 occurring mainly between 0 and 3°C (Froidurot et al., 2014) and the lower the humidity, the higher the probability of snowfall
356 is. In this study, the threshold from rain to snow was defined at $\leq 0^{\circ}\text{C}$, as below this temperature rain is almost excluded
357 (Froidurot et al., 2014; Fehlmann et al., 2018).



358 4 Results

359 4.1 Sediment-Contributing-Area (SCA) approach

360 All determined regression lines show a positive correlation between log mean annual sediment yield (SY) and log sediment
361 contributing area (SCA) (Figure 6, Appendix A), which means that SY increases with the corresponding SCA. In the following,
362 only the median of the 100 regression lines (median slope) of all AOIs and epochs is used to qualitatively describe
363 corresponding differences. Mostly, there is a decrease in SY between the different epochs and a decrease of the slopes of the
364 regression lines, which is due to a decrease in SY per square metre of the AOIs. With regard to section 3.3, a decreasing
365 intercept together with an almost constant slope close to one over the different epochs (in the log-log-model) (although with a
366 slightly decreasing slope) indicates that the relation between SCA and SY stays nearly constant. The AOI's KG3, KG4, KM1,
367 KM2 and KW2 show such a behaviour. On the other hand, the areas KG1, KG2, KG5, KW1 and MH2 show clearly larger
368 differences in the epochs. In the earliest epoch, the slopes considerably larger than one (in the log-log model) show polynomial
369 behaviour, which means that in the same AOI an increasing SCA provides clearly more SY per square meter. In the later
370 epochs, the slopes also tend towards one, so that the models of the different groups become similar. In addition to this general
371 trend (ten AOIs), an increase in SY and an increase in the slope of the regression line for AOI HG1 were observed, showing
372 an increase in sediment dynamics over the epochs in this case, which is in contrast to the previous observations. AOI MH1
373 shows a similar level of SY (between the epochs) with higher slopes of the regression lines, also indicating an increase in SY.
374 Furthermore, slopes of the regression lines below 1 occur in all epochs, but especially in the second and third.

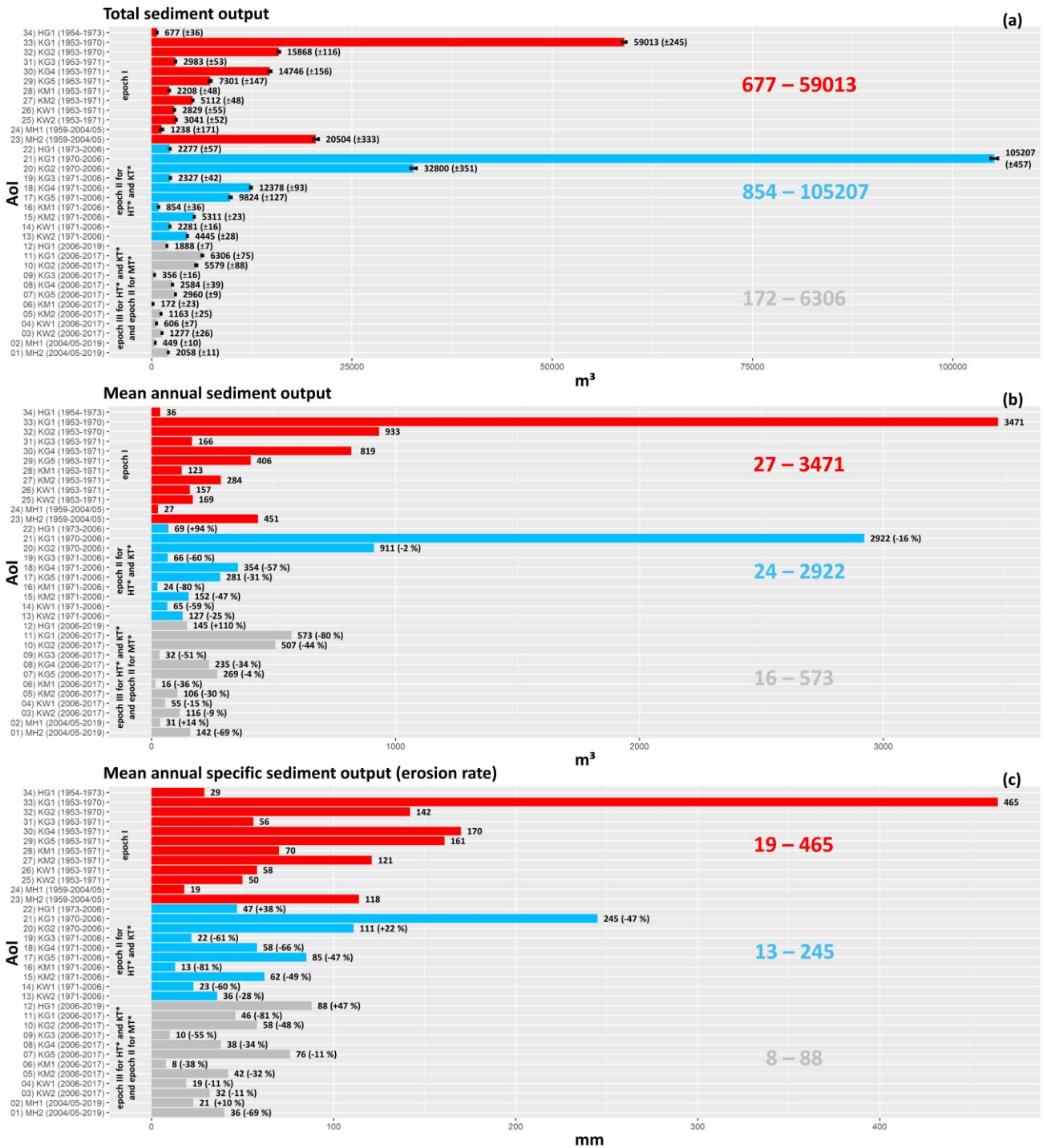


375

376 **Figure 6: Relationships between log SCA and log SY yield for 100 samples of each AOI and the corresponding epochs. In addition,**
 377 **the median regression line (median slope) is represented by a slightly thicker and darker line.**

378 **4.2 Volume calculations of the sediment output**

379 The analyses of the sediment output of the AOIs confirm the results of the SCA approach (Figure 7). In general, there is a clear
 380 and continuous decrease in mean annual SY of ten AOIs over the different epochs. In contrast to this trend, AOI HG1 shows
 381 a clear increase in mean annual SY. AOI MH1 also shows an increase, but at a very low level, which can also be described as
 382 a geomorphic activity of a similar level. In total, the mean annual sediment output decreases across the different epochs.
 383 Nevertheless, there is also very high temporal and spatial variability of this change on the AOIs HG1 and MH1, which also
 384 shows a clear increase in geomorphic activity as well as a slight increase (respectively activity at the same level).



385

386

387

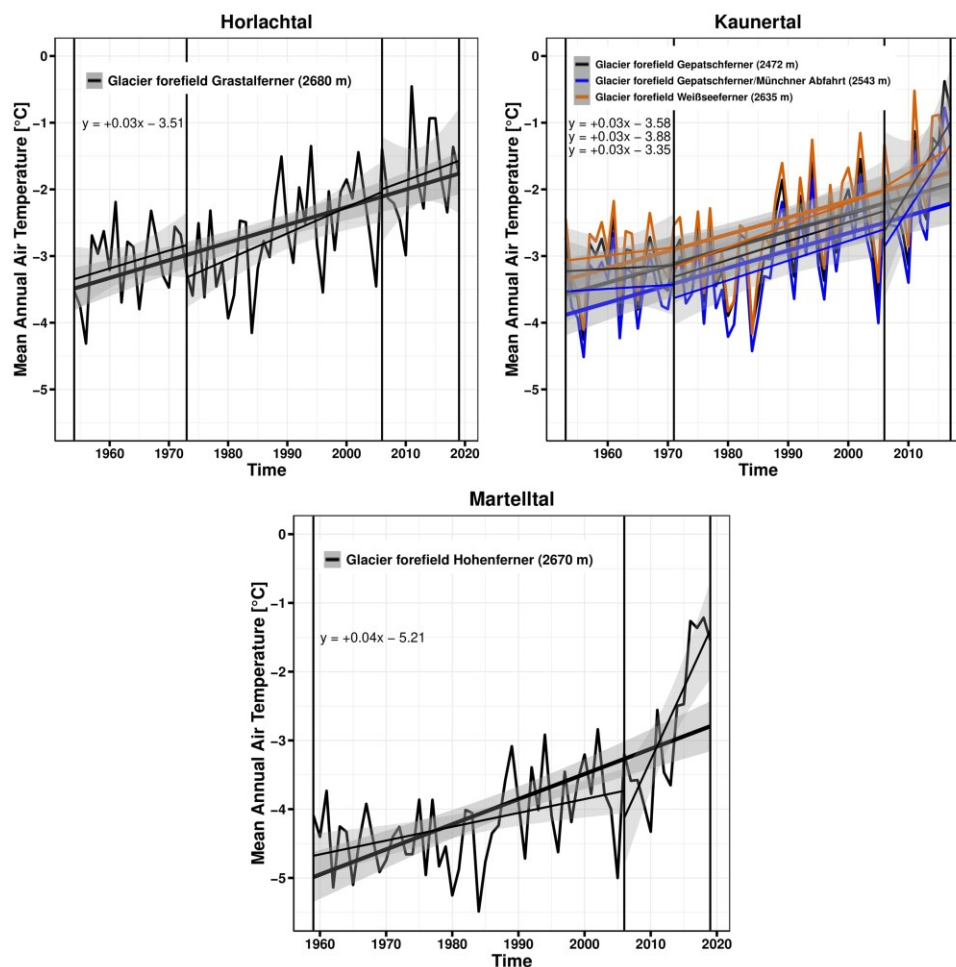
Figure 7. Bar plots of total sediment output (with error range according to Anderson (2019), see sect. 3.1.3 and 3.4), mean annual sediment output and mean annual specific sediment output (erosion rate) of each AOI and epoch.



388 4.2 Meteorological regime

389 4.2.1 Air temperature

390 The mean annual air temperature (2 m above ground) of all selected positions of the glacier forefields shows a statistically
391 significant warming trend over the entire study period of 60, 64 and 65 years (Figure 8). Overall, there is a positive total change
392 of +1.75°C (annual trend 0.03; p-value <0.05; R² 0.39) for the Horlachtal/Grastalferner glacier forefield, +1.68°C (annual trend
393 0.03; p-value <0.05; R² 0.38) for the Kaunertal/Gepatschferner glacier forefield, +1.70°C (annual trend 0.03; p-value <0.05;
394 R² 0.38) for the Kaunertal/Gepatschferner Münchner Abfahrt glacier forefield, for the Kaunertal Weißseeferner glacier
395 forefield of +1.64°C (annual trend 0.03; p-value <0.05; R² 0.36) and for the Martelltal Hohenferner glacier forefield of +2.23°C
396 (annual trend 0.04; p-value <0.05; R² 0.45).

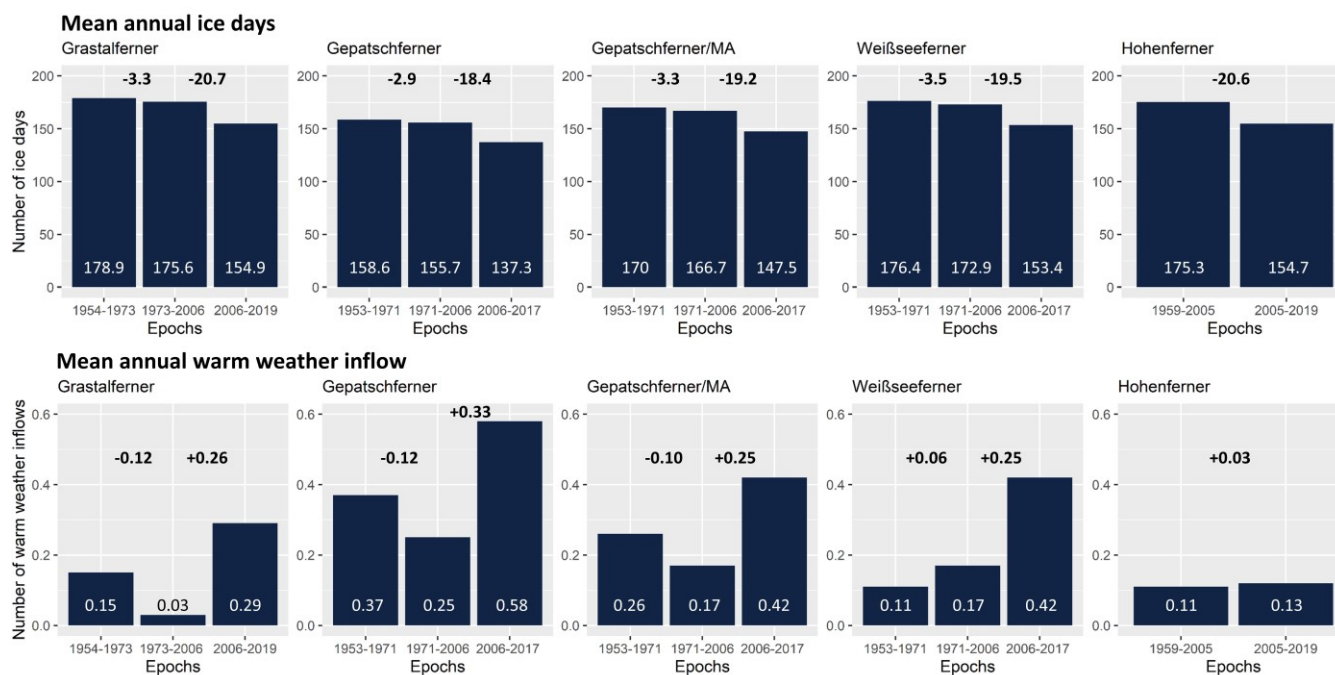


397

398 **Figure 8: Mean annual 2 meter air temperature of the glacier forefields within the study epochs (95% confidence interval is**
399 **included).**



400 The analysis of the mean annual ice days shows a decrease between the epochs, especially from the second to the third epoch
 401 (in the Martelltal from the first to the second), with a decrease in ice days between 18.4 and 20.7 days, which corresponds to
 402 almost three weeks (Figure 9). The analysis of the mean annual warm air inflows shows a decrease from the first to the second
 403 epoch in the glacier forefields of Grastalferner, Gepatschferner and Gepatschferner/MA, and a more pronounced increase from
 404 the second to the third epoch. In the glacier forefield of Weißseeferner, there is a consistent increase, the latter being equally
 405 more pronounced, whereas in Martelltal there is only a slight increase. Thus, the number of warm air inflows has generally
 406 increased.



407

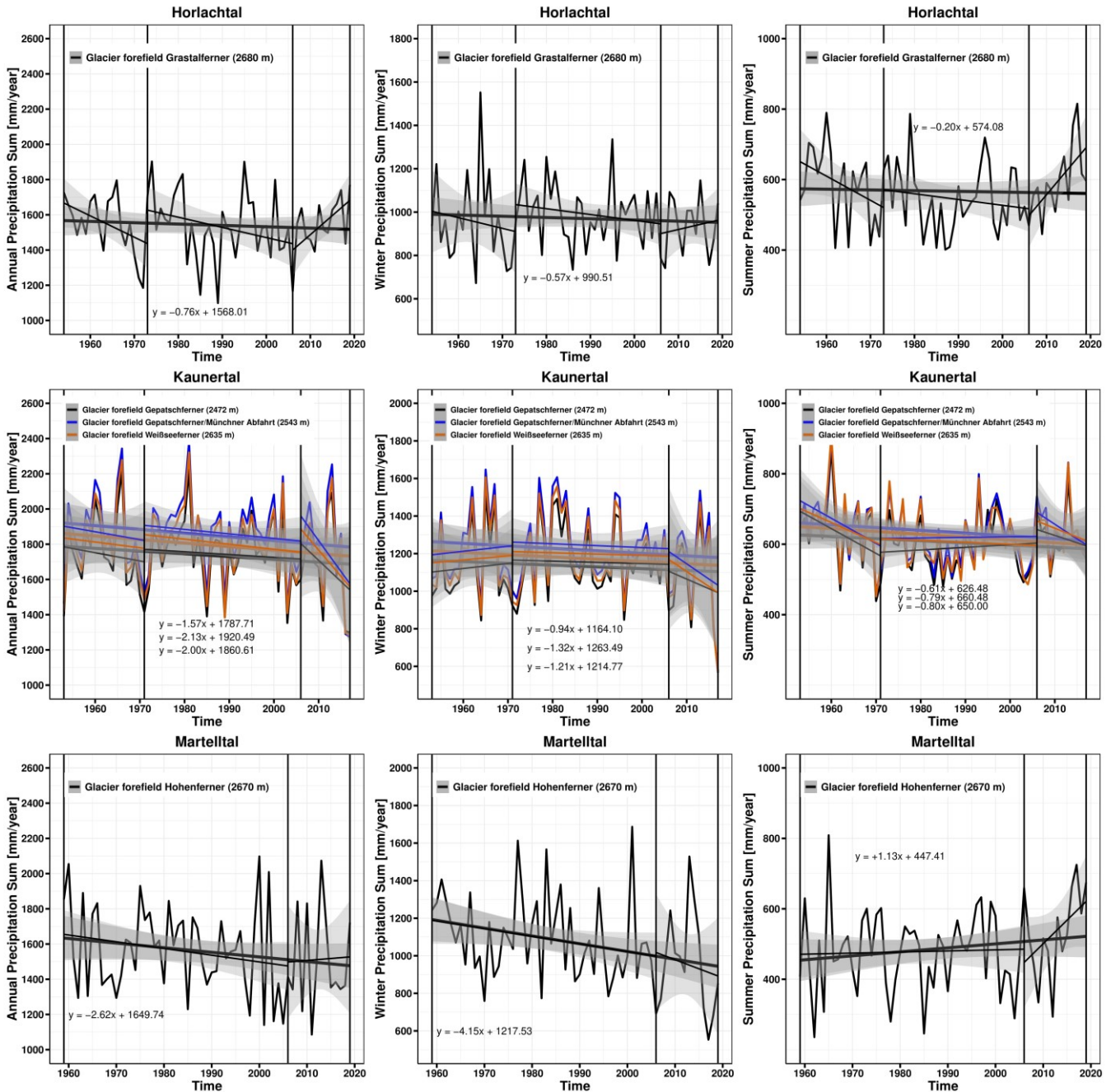
408 **Figure 9: Mean annual ice days and mean annual warm weather inflows with the corresponding changes between epochs.**

409 **4.2.2 Precipitation**

410 Over the entire epochs (60, 64 and 65 years), all study areas show a decreasing trend in mean annual, mean summer and mean
 411 winter precipitation (with the exception of summer precipitation in the Martelltal, which shows a positive trend) (Figure 10).
 412 However, only the changes in winter precipitation (entire study period), summer precipitation (second epoch: 2004/2005-2019)
 413 in the Martelltal (Hohenferner glacier forefield) and annual precipitation (third epoch: 2006-2019) in the Horlachtal
 414 (Grastalferner glacier forefield) are statistically significant, although the latter both cover only 13 and 14 years. In the
 415 Horlachtal, the first two epochs show a decreasing trend in precipitation, while the third epoch shows an increase in
 416 precipitation, which is significantly more pronounced in summer than in winter. In the Kaunertal, winter precipitation shows
 417 a slight increase in the first epoch and a stronger decrease in summer precipitation. The second epoch shows a slight increase
 418 in summer and a slight decrease in winter. The third epoch also shows a strong decrease in summer and winter precipitation.



419 In the Martelltal, on the other hand, winter precipitation decreases significantly and summer precipitation increases
 420 significantly, especially in the second epoch, although epochs of different lengths are analysed.



421

422 **Figure 10: Mean annual, mean summer and mean winter precipitation of the respective glacier forefields.**



423 In the following, the changes of different precipitation classes (as well as with a different temporal resolution) between the
424 individual epochs are analysed. The calculated changes are based on Appendix B and C. In these tables, the number of all
425 precipitation events of the corresponding epochs is shown and divided into corresponding precipitation classes. Using the
426 number of years per epoch, this results in an mean annual number of events per class. The calculated changes result from the
427 comparison of the mean occurrence of the precipitation classes of the previous epoch. Both precipitation events with a
428 resolution of one hour (Figure 11/Appendix B) and daily precipitation totals (Figure 12/Appendix C) were analysed. The
429 highest temporal resolution (1 hour) shows that the classes >0 to 4 and 4 to 8 are subject to the highest variations (Figure 11);
430 for example, precipitation events of the class >0 to 4 occur 7.63 times less in the glacier forefield of the Grastalferner in the
431 second epoch compared to the first. In general, it can be seen that the higher precipitation classes tend to decrease, albeit very
432 slightly, but there are still changes with both an increase and a decrease in the different precipitation classes. The daily
433 precipitation totals also show a high variation, with both a decrease and an increase over the different epochs (Figure 12). In
434 general, there are also very slight changes. Nevertheless, the decrease in the higher three classes predominates when comparing
435 the third with the second epoch.

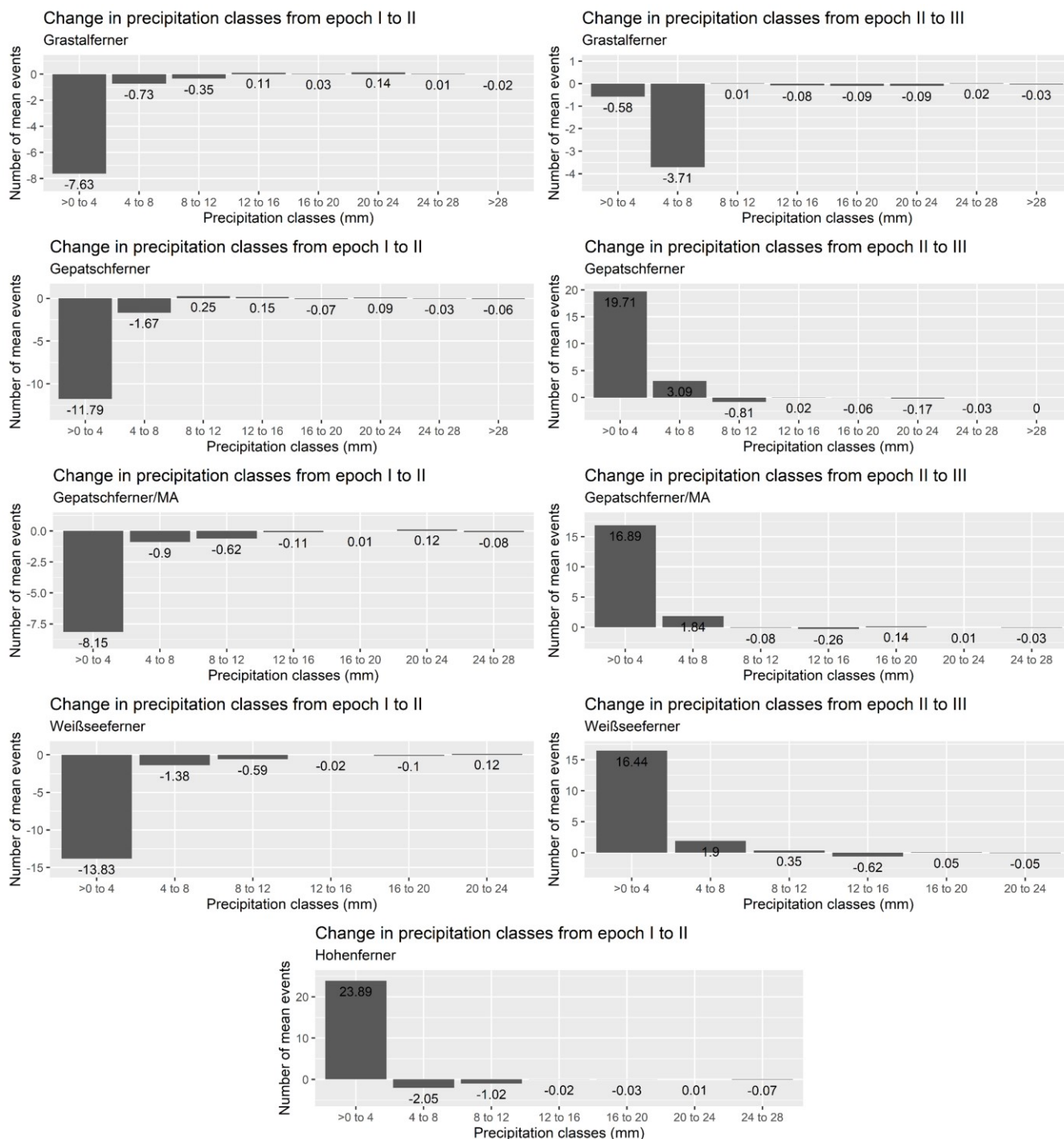
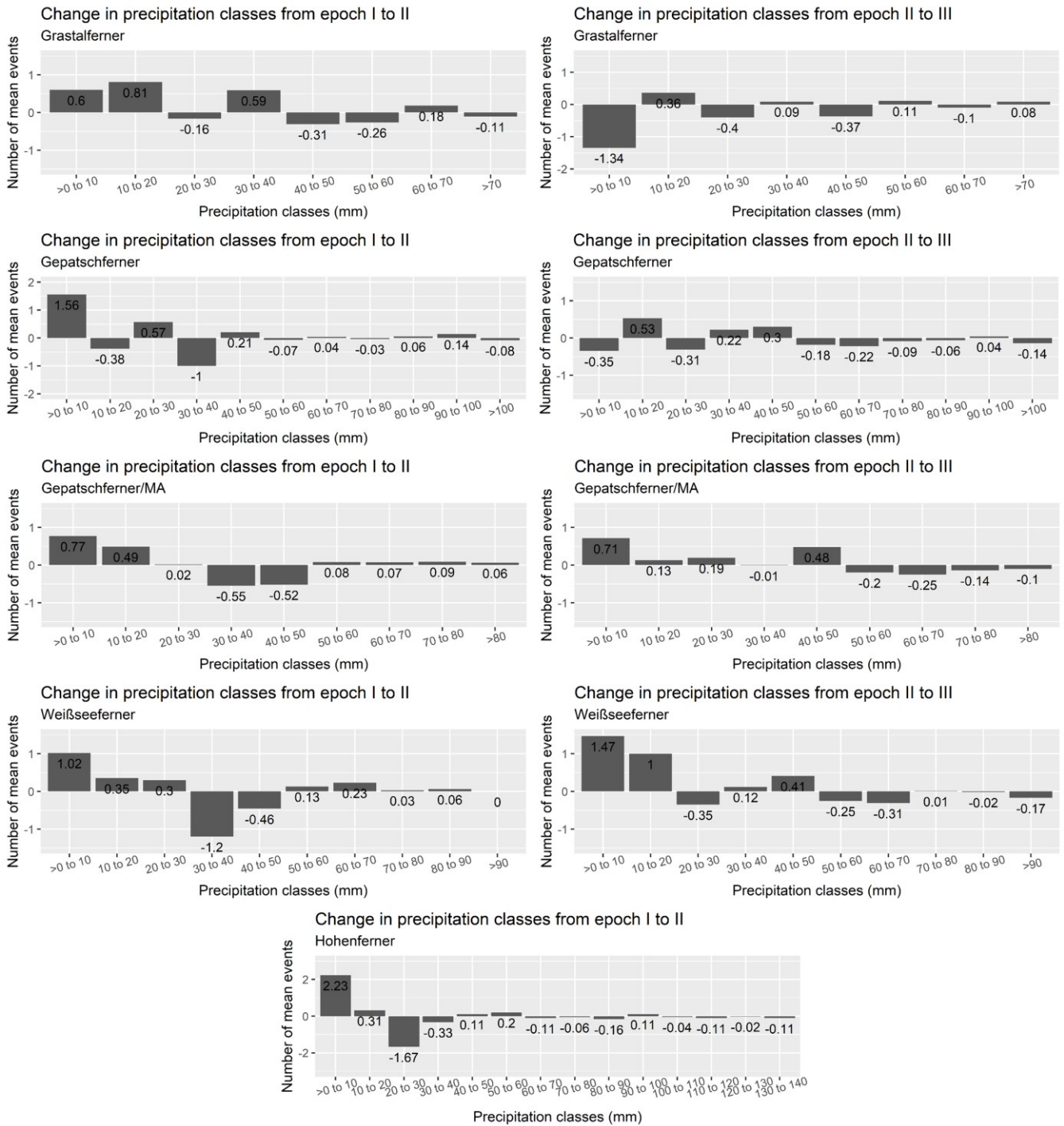


Figure 11: Change in precipitation classes between the different epochs with a one-hour resolution (extreme precipitation events).

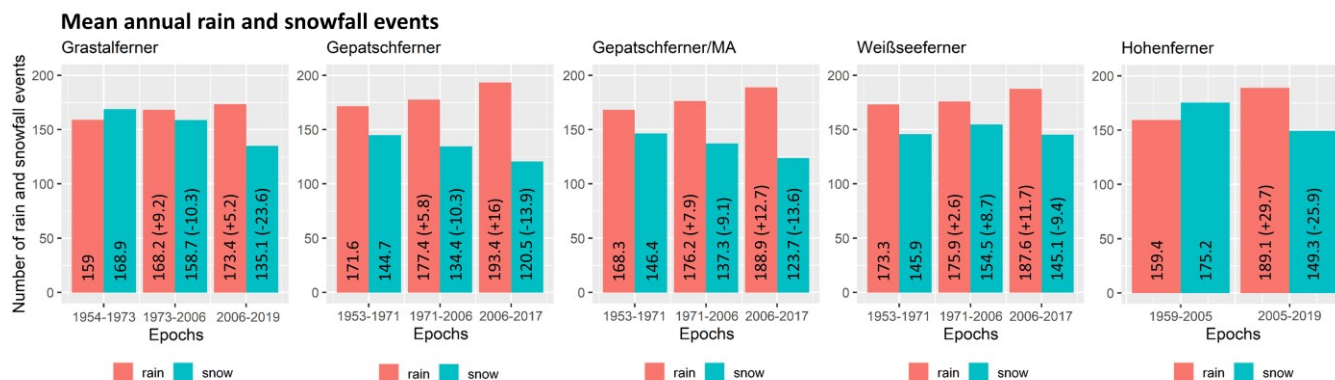


440

441 **Figure 12: Change in precipitation classes between the different epochs with a 24-hour resolution (daily precipitation totals).**



442 The analysis of the mean annual rainfall and snowfall events shows that there is a consistent increase in rainfall and at the
 443 same time a consistent decrease in snowfall (except for the Weißseeferner glacier forefield) (Figure 13).



444

445 **Figure 13: Mean annual rain and snowfall events with the corresponding changes between epochs.**

446 **5 Discussion**

447 **5.1 Assessment of the SCA approach**

448 Using the relationship between accumulated SY from DoDs and SCA/CA (log-log model) of different AOIs and different
 449 epochs, we show a long-term monitoring of several geomorphologically active sections of LIA lateral moraines. This is a clear
 450 difference to previous studies that used the space-for-time-substitution (SFTS) approach in proglacial areas, in which studies
 451 used recent morphometrical or morphodynamical differences between sites located along a gradient of deglaciation age to
 452 infer long-term changes in morphodynamics (Ballantyne and Benn, 1994; Curry, 1999; Curry et al., 2006). Means that long-
 453 term studies with quantitative data are rare (Schiefer and Gilbert, 2007; Betz et al., 2019; Altmann et al., 2020; Betz-Nutz,
 454 2021; Betz-Nutz et al., 2022). The approach shown here provides reliable results and requires only a few input data (Neugirg
 455 et al., 2015a; 2015b; 2016; Dusik, 2019; Dusik et al., 2019). The results mainly show a decrease in SY as well as a decrease
 456 in the slope of the regression lines (suggesting less SY per square metre) over the different epochs, indicating a decrease in
 457 geomorphic activity on these AOIs. In some AOIs, we observe contrasting changes: There is an increase in SY and an increase
 458 in the slope of the regression line at HG1 and almost no change in SY on the Y-axis but an increase in the slope of the regression
 459 line at MH1, which can be described as an increase (HG1) and a constant geomorphic activity (MH1). Moreover, in the earlier
 460 epochs, a clearly higher variability of SY (Slope of the regression line clearly higher 1) was observed on the respective AOIs,
 461 which is no longer reached in the later ones. Thus, it is possible to describe two different types of change in SY (size of SY
 462 between epochs and variability of SY within an epoch, which can also be compared with the other epochs). Slopes of the
 463 regression line below 1 could occur when spots appear within the area that are no longer active, which could be an indication
 464 of stabilisation, which occurs mainly in the second and third epoch.

465



466 The p-values of the coefficients are mostly below the alpha level of 0.05, so it is assumed that the relationships between SCA
467 and SY are statistically significant in almost all cases (~92%) (Figure 6). To determine the proportion of the variance of the
468 dependent variable that can be explained by the independent variable, the R-squares (R^2 or the coefficient of determination) of
469 all regression lines were analysed (Figure 6, Appendix A). The relationship between SCA and SY shows varying correlations
470 within the AOI and the epochs. The median R^2 values range from 0.59 to 0.91 in the first epoch, from 0.37 to 0.93 in the second
471 epoch and from 0.3 to 0.94 in the third epoch (Figure 6, Appendix A). The number of channels modelled differed between the
472 epochs on the same AOIs due to the different quality of the DEMs and the slightly different size of these. As in Heckmann
473 and Vericat (2018), the accumulation of DoD values resulted in very small positive values at some AOIs. Such errors are due
474 to the quality of the DoD, different bulk densities of eroded vs. deposited materials, and the inability of the flow routing
475 algorithm to fully reproduce sediment transfer in reality especially when flow directions changed within one epoch. Where
476 positive accDoD values occurred, they were small and manually corrected to the zero.

477 Nevertheless, the D8 algorithm simplifies complex sediment transport processes such as fluvial activity, landslides and debris
478 flows, which have different frequencies, magnitudes and forms of erosion and accumulation. As the individual epochs cover
479 several years, no reference can be made in this study to individual processes that can be attributed to extreme precipitation
480 events or to seasonal differences. Therefore, we compare different epochs based on mean annual SY, which includes all
481 geomorphological processes. Accordingly, the aim was not to model individual erosion processes but to compute SY of each
482 cell. The individual AOIs have a slightly different area within the different epochs, which is mainly due to headcut retreat
483 (Heckmann and Vericat, 2018; Betz-Nutz et al., 2022). The lateral boundaries also changed slightly due to the quality of the
484 DEMs and geomorphological slope processes, while the lower boundary did not change.

485 By processing historical aerial photographs into DEMs (by SfM-MVS), the temporal aspect of SCA studies could be quickly
486 and cost-effectively extended to several decades (up to the 1950s), which previously spanned only a few months or several
487 years (Neugirg et al., 2015a; 2015b; 2016; Dusik, 2019; Dusik et al., 2019). However, as Schiefer and Gilbert (2007) have
488 already shown, the shorter the time intervals and the lower the quality of the aerial images, the more difficult it becomes to
489 detect surface changes, so in the process of this study several series of aerial images had to be sorted out that were actually
490 available due to a poor data quality. Furthermore, it should be noted that the accuracy and precision of the historical DEMs
491 strongly depends on the respective generation, e.g. whether they were generated with or without a calibration certificate (as
492 was the case, for example, with the 1959 aerial photo series in the Horlachtal/glacier forefield Hohenferner), which ultimately
493 influences the SCA results and the calculated erosion rates (Stark et al., 2022).

494 **5.2 Geomorphic activity**

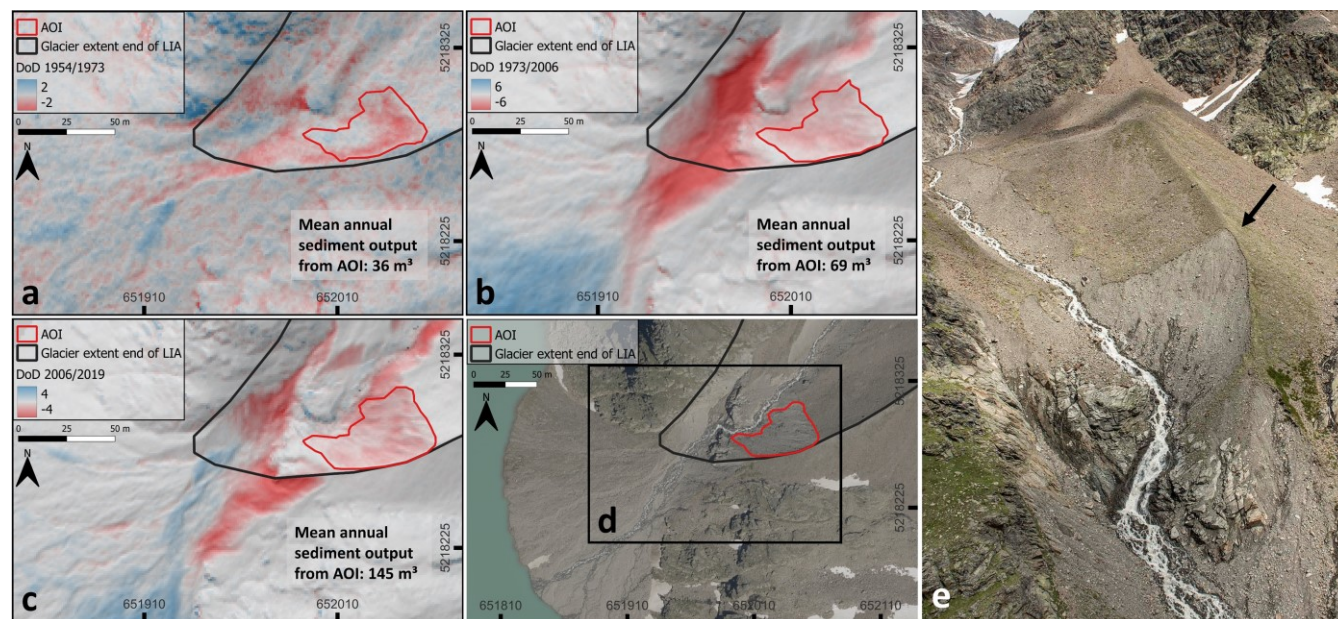
495 The geomorphic activity is directly related to the characteristics of the AOIs. The AOIs with the highest mean annual sediment
496 output ($>100\text{m}^3/\text{a}$) (such as KG1, KG2, KG4, KG5, MH2, KM2, KW2) show strong gully formation and are overall
497 characterised by larger areas, longer max. slope lengths and higher mean and max. slope gradients (Table 1). In contrast, the
498 AOIs with lower mean annual sediment output ($<100\text{m}^3/\text{a}$) (such as KW1, KG3, HG1, KM1, MH1) show less gully incision.



499 These AOIs tend to be characterised by smaller areas, smaller max. slope lengths and smaller mean slope and max. slope
500 gradients (Table 1). The strong influence of slope length and slope gradient on morphodynamics is also shown by previous
501 studies (Ballantyne and Benn, 1994; Curry, 1999; Curry et al., 2006; Betz-Nutz et al., 2022). KG3 also appears to be somehow
502 stabilized by bedrock in the lower part of the slope, which could mitigate the erosion of this AOI. Elevation and aspect,
503 however, do not seem to have an influence on geomorphic activity, which is also shown in the study by Curry et al. (2006).
504 Since only bare and sparsely vegetated areas were investigated, no findings on the influence of vegetation on morphodynamics
505 can be made in this study. Solifluction processes could also not be observed, probably due to the composition of the moraine
506 material. Presumably, the morphodynamics are still so high that the vegetation does not yet have the opportunity to develop
507 accordingly. In general, we assume that debris flows are the most common process, as described for example by Ballantyne
508 (2002a) and Curry et al. (2006). Thus, material stored in the gullies is transported downslope by debris flows mainly rain or
509 snow events in the spring or heavy rainfall events during rainstorms in the summer months (Ballantyne and Benn, 1994;
510 Ballantyne, 2002b; Curry et al., 2006; Dusik et al., 2019).

511 However, the high mean annual sediment yield and corresponding erosion rate in the first (3471 m³/a, 465 mm/a) and second
512 (2922 m³/a, 245 mm/a) epochs of AOI KG1 (Figure 7) can probably also be attributed to individual landslides and deep-seated
513 slope failures in some cases linked with melting dead ice bodies, as these processes are more likely to occur after deglaciation,
514 and are characterised by high magnitude and low frequency, which has also been shown by Blair (1994), Hugenholtz et al.
515 (2008) and Cody et al. (2020). On the less incised slopes (e.g. MH1), small-scale processes such as fluvial erosion or snow
516 drifts probably occur (Betz-Nutz, 2021), which ultimately show no clear trend in the increase or decrease of morphodynamics,
517 but can be described as a constant geomorphic activity. In Betz-Nutz et al. (2022) and in this study, six similar lateral moraine
518 sections (although other exactly defined AOIs) were investigated. The test sites KG1, KG2, KW1, KW2 and MH1 (in Betz-
519 Nutz et al. (2022): GPF1, GPF2, WSF1, WSF2 and HF1) showed similar erosion rates and the same log-term trends. In the
520 case of AOI MH2, different trends were determined (stagnation in Betz-Nutz et al. (2022) and a decrease in this study), which
521 can be attributed to the differently defined AOI and the slightly different study period.

522 In the sense of a process-response system, it is noticeable that the first-mentioned group of AOIs with the higher erosion rates
523 (except KG1) had considerable influence from melting dead ice in the lower slope area at least until 2006 (KG2, KM2, KW2,
524 MH2) or the glacier was still present at the bottom of the slope (KG4, KG5), which could be identified by the interpretation of
525 the DoDs. Melting of the dead ice can lead to destabilisation of the slope, which can enhance erosion processes of the upper
526 slope areas, as the support is no longer present, the sediment becomes saturated and there can be an increase in the slope
527 gradient due to the subsidence of the lower part of the slope (Altmann et al., 2020; Betz-Nutz et al., 2022). However, the
528 highest slope gradients are also present here, which also plays a major role. In addition, AOI HG1, where erosion is increasing,
529 shows an undercutting of the slope by the adjacent stream, which leads to a destabilization or lowering of the erosion base and
530 a typical formation of a debris cone and alluvial fan with a successive reduction of the slope gradient is missing (Figure 14).
531 It can be assumed that individual strong rainfall events in the second and third epochs in combination with changing flow
532 pathes due to the retreat of the Grastalferner acted here as an impulse and affected both the AOI itself and the adjacent stream.



533

534 **Figure 14: Overview of the DoDs of the corresponding epochs of AOI HG1: (a) DoD 1954-1973, (b) DoD 1973-2006, (c) DoD 2006-**
 535 **2019, (d) Orthofoto 2020 (provided by the Province of Tyrol) and (e) photo of the AOI from 2019 by Anton Brandl.**

536 5.3 Paraglacial landscape adjustment

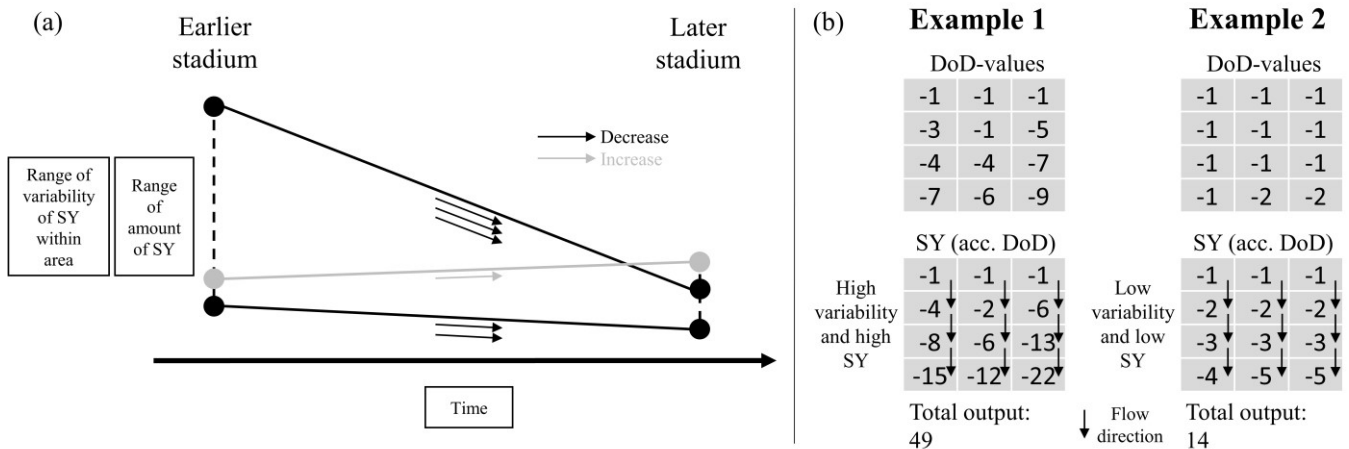
537 5.3.1 The "Sediment activity concept"

538 The finding of mainly decreasing geomorphic activity of LIA lateral moraines in this study is largely consistent with previous
 539 model-based studies describing the paraglacial landscape adjustment with a decrease in geomorphic activity in proglacial areas
 540 over time, such as the theoretical model "paraglacial concept" of Church and Ryder (1972) or the "sediment exhaustion model"
 541 of Ballantyne (2002a, 2002b). The geomorphic activity of gully systems is given as a few decades to centuries (Ballantyne,
 542 2002a; 2002b). Furthermore, it is stated that there is a high temporal and spatial variability in this development. The model
 543 provides an appropriate approximation (Ballantyne, 2002a; 2002b). Within the paraglacial adjustment process, different
 544 geomorphological processes result in different durations of occurrence. Furthermore, different land systems react at different
 545 rates and on different spatial scales. Thus, external perturbations can occur, leading to secondary peaks and time delays
 546 (Ballantyne, 2002a; 2002b). While ten out of twelve AOIs fit the model descriptions, two test plots show opposite
 547 morphodynamics, which can be described as a delay of the paraglacial adjustment process or that response systems can run
 548 counter to such an adaption.

549 To estimate the changing morphodynamics, we therefore propose the following simplified description of the landscape
 550 evolution using the "Sediment activity concept" based on the results of this study. Due to the study design, this concept is only
 551 valid on geomorphologically active areas (in this case the upper lateral moraine section) on LIA lateral moraines and until
 552 about 170 years after the end of LIA (Table 6, Figure 15). The concept distinguishes between an earlier and a later phase. The



553 earlier phase (mainly 1950s to 1970s) is characterised by a wide range between areas with high and low variability of SY
 554 within the area as well as high and low mean annual sediment yield (erosion rate/volume). In contrast, the later stadium (mainly
 555 1970s to 2000s and 2000s to the end of the survey 2017/2019) shows a decrease in this range. Although the decrease of
 556 morphodynamics predominates, there are also increases in morphodynamics. The time of ice release was not integrated here,
 557 so that the time periods refer to the actual time. In addition, we give two examples in Figure 15. While example A shows high
 558 variability (polynomial behaviour) within the area and high SY (erosion rates/sediment output), example B shows low
 559 variability (constant/linear behaviour) and low SY (erosion rates/sediment output). Ultimately, the relationship between SY
 560 and the size of the catchment has changed so that erosion within the area is more constant today.



561

562 **Figure 15: The "Sediment activity concept". Description and illustration of the change in sediment activity over time (a) and 2**
 563 **corresponding examples (b).**

564 **Table 6: Tabular summary of the simplified conceptual model.**

	Earlier stadium	Later stadium
SY within area	highly variable up to constant	in the range of constant
Amount of SY	wide range	lower range
Over time	mostly decreasing	

565

566 Introducing the "Sediment activity concept" of this study, we present a different description of the paraglacial adjustment
 567 process which is based on the actual SY. However, the concept is only valid until about 170 years after the end of LIA and on
 568 the AOIs of this study. Nevertheless, we assume that the concept can also prove its validity in further proglacial active areas
 569 and partly over an even longer period of time.



570 **5.3.2 Erosion rates**

571 The comparison of long-term erosion rates of gully systems in proglacial areas of different studies shows the high variability
 572 of this adjustment; as these studies were carried out with different methods, on different time scales and in different glacier
 573 forefields, comparing their results is difficult (Table 7). The methodologies for determining long-term average erosion rates
 574 are based on gully volume estimates (Ballantyne and Benn, 1994; Curry, 1999; Curry et al., 2006) and sediment volume
 575 calculations due to surface changes using DoDs, as shown by Betz-Nutz et al. (2022) and this study. In glacier forefields in
 576 western Norway, this amounts e.g. to minimum estimates of 50-100 mm/year (max. estimates of min. 200 mm/year)
 577 (Ballantyne and Benn, 1994) and a minimum of 5.5-169 mm/year (in different glacier forefields) (Curry, 1999). A further
 578 study in the Swiss Alps shows erosion rates of min. 49-151 (in different glacier forefields) (Curry et al., 2006). The work of
 579 Betz-Nutz et al. (2022) and this study show erosion rates over several decades and distinguish between different epochs, which
 580 makes it possible to show differences between them. Both studies show that the mean erosion rates in the individual epochs
 581 decrease (Table 7), although in individual cases there is also a constant and an increase in erosion rates over time. Although
 582 there has been a clear decrease in geomorphic activity, stabilisation of the AOIs is not yet apparent, which means that the
 583 paraglacial adjustment is still ongoing. Within this study, we observed that the AOIs still show a high geomorphic activity
 584 even after they have been deglaciated for 76-159 years. A stabilisation of the gully systems as shown by Curry (2006) cannot
 585 be observed. Other studies such as Lane et al. (2017), Dusik (2019), Altmann et al. (2020), Betz-Nutz et al. (2022) also show
 586 the still ongoing paraglacial adjustment processes.

587 **Table 7: Studies on long-term erosion rates (several decades) of gully systems on LIA lateral moraines in different glacier forefields.**

Study	Erosion rate (mm/year)	Timescale (year)	Time since ice exposure (year)	Location of the study area
Ballantyne and Benn (1994)	Min. of 50-100, max. min. of 200	48	48	Norway, Fåbergstølsbreen
Curry (1999)	Min. of 5.5-8.8, 38- 169 and 19-169	76, 53, 43	76, 53, 43	Norway, Fåbergstølsbreen, Lodalsbreen and Heillstugubreen
Curry et al. (2006)	Min. of 86-151 and 49-103	55, 79	55, 79	Switzerland, Glacier du Mont Miné and Feegletscher
Betz-Nutz (2021; 2022)	Epoch I: 2-429, epoch II: 1-186, epoch III: 3-110	Epoch I: Mainly ~1950s to ~1970s, Epoch II: ~1970s to ~2000s and Epoch III: ~2000s to 2018/2019	59-154	Austria (Tyrol), Germany (Bavaria) and Italy (South



This study	Epoch I: 19-465, epoch II (HT and KT): 13-245, epoch II (MT) and epoch III (HT and KT): 8- 88	Epoch I: 17-19 (in HT and KT) and 45/46 (in MT), epoch II: 33-36 (in HT and KT) and 14/15 (in MT) and epoch III: 11-13 (in HT and KT)	76-159	Tyrol), ten different glacier forefields Austria (Tyrol) and Italy (South Tyrol), five different glacier forefields
------------	--	---	--------	--

588 *HT = Horlachtal, KT = Kaunertal and MT = Martelltal.

589 **5.4 Meteorological drivers**

590 The decrease of the mean annual number of ice days and the increase in the number of warm spells over the different epochs
 591 and the associated potential increase in snowmelt on the slopes could also lead to an increase in morphodynamics, as these
 592 processes represent important preparatory steps for erosion processes in spring (Haas, 2008), such as increased saturation of
 593 the slope due to snow melt, loosening of the upper sediment layers or the delivery of material by snow slides or small wet
 594 avalanches that is then available for debris flows in the summer months (Dusik et al., 2019). Klein et al. (2016), for example,
 595 also show an increase in the frequency and intensity of snowmelt in the Swiss Alps. Mean annual precipitation decreases
 596 slightly across epochs, but is not statistically significant (except for winter precipitation for the entire study period (1959 to
 597 2019) and summer precipitation in the second epoch from 2005 to 2019 in the Martelltal). Other studies also show that the
 598 decrease in precipitation in the Alps is low (Brugnara et al., 2012) and that there is no clear trend in precipitation (Hock et al.,
 599 2019) or that it is mainly subject to regional influences and decadal variations (Mankin and Diffenbaugh, 2015). Extreme
 600 precipitation events (1h resolution) and daily precipitation totals also show only minor changes. Differentiation of
 601 precipitation, on the other hand, shows a clear increase in rainfall and a decrease in snowfall, which is also shown by Serquet
 602 et al. (2011), Beniston et al. (2018) and Hock et al. (2019) who found that the rainfall on snow events in spring as preparatory
 603 factor for the erosion processes in the summer months increase. The simulated meteorological data generally show lower
 604 temperatures and larger precipitation amounts, when compared to three automatic weather stations operated by TIWAG
 605 (Tyrolean Hydropower AG, Innsbruck, Austria). These stations are located in the vicinity of our AOIs. The simulated mean
 606 annual temperatures extracted at the location of the weather stations Horlachalm (1987-2015) (approx. 6.5 km linear distance
 607 to the AOI in the Grastalferner glacier forfield) and Weißseeferner (2007-2015) (approx. 500 m linear distance to the AOIs in
 608 the Weißseeferner glacier forfield), covering the same time period indicate a difference of -1.05°C and of -0.87°C, respectively,
 609 after accounting for differences in elevation. However, at Gepatschalm (2010-2015) weather station (approx. 2.5 km linear
 610 distance to the AOIs in the Gepatschferner glacier forfield), the difference between the simulated and observed mean annual
 611 temperatures is 0.13°C, indicating that the magnitude of the discrepancies depends on the station data used for the comparison.
 612 The simulated precipitation, however, is generally larger with mean annual precipitation sums of 1531, 1655, and 1820 mm at
 613 the location of Horlachalm (1990-2015), Gepatschalm (2010-2015), and Weißseeferner (2007-2015), respectively, while the



614 weather stations recorded values of 803, 1086, and 924 mm, indicating large discrepancies especially when compared to
615 Horlachalm and Weißseeferner weather stations. The datasets from which the temperature and precipitation were extracted are
616 both based on coarsely resolved data, which makes a comparison with measurement data in the field difficult, although the
617 corresponding trends are well usable for this study. The large difference between simulated and recorded precipitation is mainly
618 due to winter precipitation (Figure 11) when the weather stations are not always able to record total snowfall accurately;
619 additionally, fog precipitation or precipitation in combination with stronger winds are not recorded correctly.

620 The weather and climate study periods are based on the predefined study epochs given by the availability and quality of
621 orthophotos, and not on the usual climate periods. This results in large differences in the length of the different epochs, which
622 must be taken into account.

623 There are several sources of uncertainty in the simulated data, amongst them the dynamic initial and boundary conditions, as
624 the forcing data have their own sources of uncertainties. Furthermore, the choice of the reanalysis data used for forcing the
625 model has an influence on the final results. Additionally, for such long simulations, an updated sea surface temperature (SST)
626 is recommended. Since there are no SSTs available for the 20CRv3, we have generated SST fields from the skin temperature.
627 Other sources of uncertainty are the static boundary conditions like the fixed land use categories and topography, as well as
628 model simplifications and choices in the parameterization of the physics and dynamics. In our simulations, we have used
629 spectral nudging in order to keep the model from large deviations from the forcing data. Short test runs indicate that the use of
630 spectral nudging improves the simulated data, especially with respect to precipitation. However, the strength of nudging also
631 has an influence on the final results. Since the purpose of this study is not to test how strongly to nudge, we have used the
632 default values in WRF.

633 **6 Conclusion**

634 Using DoDs based on SfM photogrammetric and LiDAR data DEMs, we show with two different approaches, the long-term
635 (1953-2019) change in the morphodynamics of several active gully systems on LIA lateral moraines in the Tyrolean and South
636 Tyrolean Alps, Austria and Italy. First, the change in the range of variability of SY within the area (using regression lines with
637 accSY and SCA/CA) and second, the change in the amount of SY (calculation of erosion rates/volume of sediment output)
638 between the different epochs could be shown.

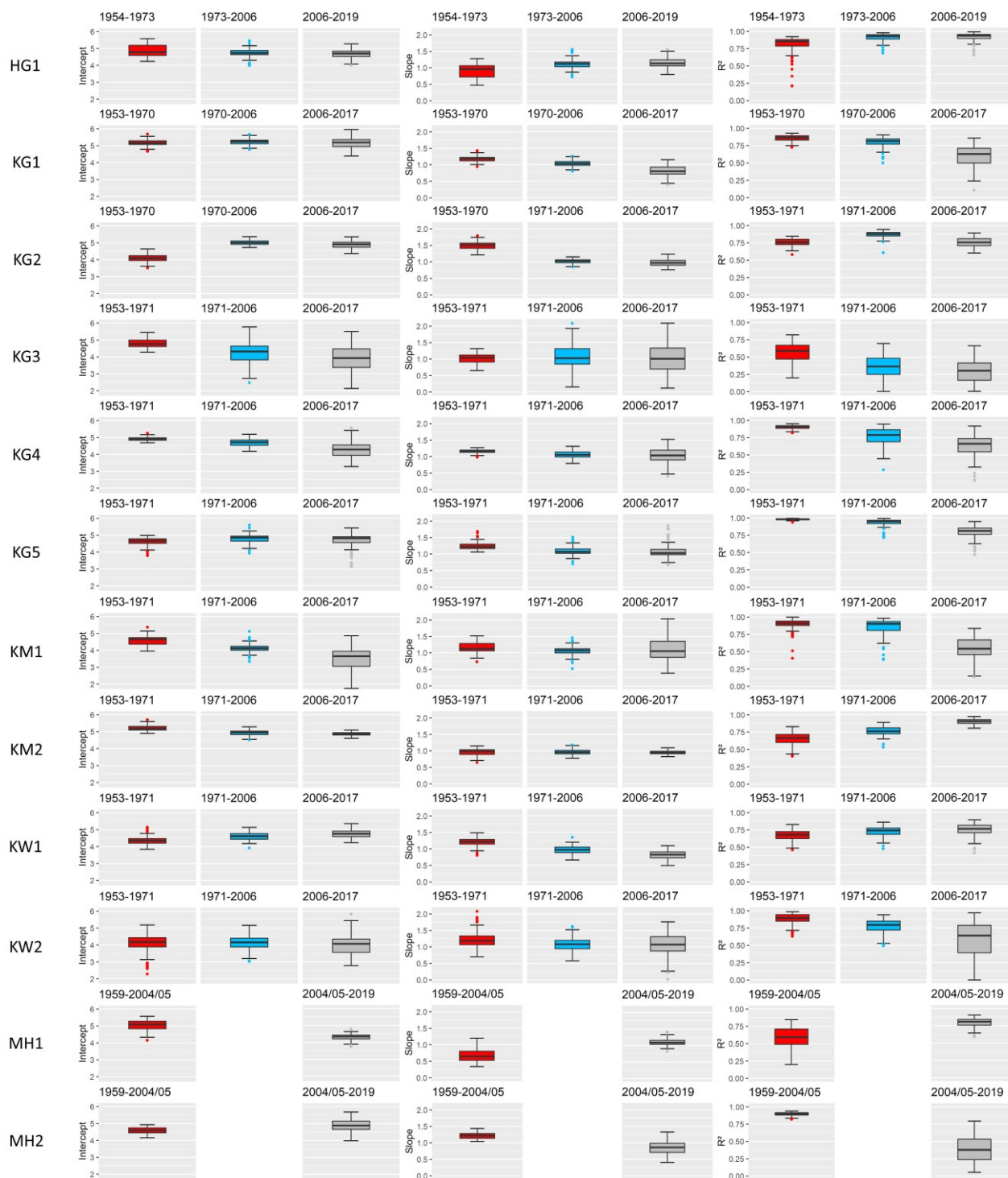
639 Finally, the first epoch shows a clearly higher range of variability of SY within the AOI than the later epochs. This means that
640 the spatial pattern of erosion has become more uniform within the areas. In addition, the total sediment yield, the mean annual
641 sediment yield and the mean annual specific sediment yield (erosion rate) were calculated for each AOI and epoch was
642 calculated. Over the epochs, there is a decreasing trend of geomorphological activity in 10 out of 12 AOIs, while 2 AOIs show
643 an opposite trend, where morphodynamics increase or remain at the same level. Overall, we confirm the general trend of
644 decreasing morphodynamics over time (10 AOIs) of several previous studies, although we could also show that the geomorphic
645 activity of one AOI is on the same level and one is increasing. Finally, the results led to the proposal of a simplified conceptual



646 model “The sediment activity concept”, describing the paraglacial adjustment process by summarising the findings on the
647 long-term morphodynamics of the upper parts (gully heads) of lateral moraines from this study.
648 Despite the general decline in morphodynamics, the AOIs show no stabilisation, leading us to the conclusion that the
649 paraglacial landscape adjustment is still in progress (even on areas that have been ice-free for at least 159 years). It seems that
650 the vegetation has not yet had the opportunity to develop due to the high morphodynamics. In general, debris flows are probably
651 the most common processes, although it is difficult to separate the different processes, but very high SY (mainly in the first
652 epoch) also indicate landslides and slope failures. AOI morphodynamic is also related to the characteristics, i.e. AOIs that are
653 larger, have longer max. lengths and higher mean slope gradients (as well as max. slope gradients) have clearly higher
654 geomorphic activity and form more deeply incised gullies. In the sense of a process-response system, it can be stated that the
655 melting of dead ice in the lower slope area, which in some cases lasts for decades, leads to high morphodynamics of the upper
656 slope area. Furthermore, it is assumed that the lowering of the erosion base by adjacent streams leads to a delay of the
657 paraglacial landscape adjustment, as the formation of an accumulation area is disrupted.
658 In addition to the system-internal influences on morphodynamics, we assume an additional influence of changing weather and
659 climate factors on the corresponding erosion processes with an increase (mainly in the last, i.e. most recent epoch from the
660 mid-2000s to 2017/2019), since the statistically significant warming of the last decades has led to a reduction of the mean
661 annual ice days, to an increase in warm air inflows and, when distinguishing between rainfall and snowfall, to an increase in
662 rainfall. We do not see any clear influence in the changing precipitation, although it can be assumed that the same precipitation
663 intensities led to higher erosion in the first epoch than in the second or third. Nevertheless, the system-internal dynamics and
664 the general paraglacial adaptation process seem to have the greatest impact on the changing morphodynamics. Future work
665 should apply the approach used here to more areas and, if possible, with a higher temporal resolution to improve the process
666 understanding of erosion on lateral moraines.



667 **Appendix A**



668
 669 **Boxplots of the model parameters Intercept, Slope and R² of all regression lines (see Figure 6).**



670 **Appendix B**

671 **Calculation of the individual extreme events by continuous ongoing 4 mm classes (with one-hour resolution).**

	Precipitation interval (mm)	No. events/total	No. events/year	No. events/total	No. events/year	No. events/total	No. events/year	Change from previous epoch	
Grastalferner (Horlachtal)		1954-1973 (epoch I)		1973-2006 (epoch II)		2006-2019 (epoch III)		I to II	II to III
	>0 to 4	6084	320.21	10315	312.58	4056	312.00	-7.63	-0.58
	4 to 8	368	19.37	615	18.64	194	14.92	-0.73	-3.71
	8 to 12	78	4.11	124	3.76	49	3.77	-0.35	0.01
	12 to 16	17	0.89	33	1.00	12	0.92	0.11	-0.08
	16 to 20	7	0.37	13	0.39	4	0.31	0.03	-0.09
	20 to 24	2	0.11	8	0.24	2	0.15	0.14	-0.09
	24 to 28	1	0.05	2	0.06	1	0.08	0.01	0.02
	>28	1	0.05	1	0.03	0	0.00	-0.02	-0.03
Gepatschferner (Kaunertal)		1953-1971 (epoch I)		1971-2006 (epoch II)		2006-2017 (epoch III)		I to II	II to III
	>0 to 4	5498	305.44	10278	293.66	3447	313.36	-11.79	19.71
	4 to 8	390	21.67	700	20.00	254	23.09	-1.67	3.09
	8 to 12	87	4.83	178	5.09	47	4.27	0.25	-0.81
	12 to 16	20	1.11	44	1.26	14	1.27	0.15	0.02
	16 to 20	9	0.50	15	0.43	4	0.36	-0.07	-0.06
	20 to 24	3	0.17	9	0.26	1	0.09	0.09	-0.17
	24 to 28	1	0.06	1	0.03	0	0.00	-0.03	-0.03
	>28	1	0.06	0	0.00	0	0.00	-0.06	0.00
Gepatschferner/ Müchner/ Abfahrt (Kaunertal)		1953-1971 (epoch I)		1971-2006 (epoch II)		2006-2017 (epoch III)		I to II	II to III
	>0 to 4	5452	302.89	10316	294.74	3428	311.64	-8.15	16.89
	4 to 8	402	22.33	750	21.43	256	23.27	-0.90	1.84
	8 to 12	96	5.33	165	4.71	51	4.64	-0.62	-0.08
	12 to 16	23	1.28	41	1.17	10	0.91	-0.11	-0.26
	16 to 20	4	0.22	8	0.23	4	0.36	0.01	0.14
	20 to 24	1	0.06	6	0.17	2	0.18	0.12	0.01
	24 to 28	2	0.11	1	0.03	0	0.00	-0.08	-0.03
Weißseeferner (Kaunertal)		1953-1971 (epoch I)		1971-2006 (epoch II)		2006-2017 (epoch III)		I to II	II to III
	>0 to 4	5690	316.11	10580	302.29	3506	318.73	-13.83	16.44
	4 to 8	408	22.67	745	21.29	255	23.18	-1.38	1.90
	8 to 12	96	5.33	166	4.74	56	5.09	-0.59	0.35
	12 to 16	23	1.28	44	1.26	7	0.64	-0.02	-0.62
	16 to 20	9	0.50	14	0.40	5	0.45	-0.10	0.05
Hohenferner (Martelltal)		1959-2005 (epoch I)		2005-2019 (epoch II)				I to II	
	>0 to 4	14531	315.89			4757	339.79	23.89	
	4 to 8	883	19.20			240	17.14	-2.05	
	8 to 12	241	5.24			59	4.21	-1.02	
	12 to 16	57	1.24			17	1.21	-0.02	
	16 to 20	8				2	0.14	-0.03	
	20 to 24	3	0.07			1	0.07	0.01	
24 to 28	3	0.07			0	0.00	-0.07		



673 **Appendix C**

674 **Calculation of the daily precipitation totals by continuous ongoing 4 mm classes of the different epochs (24-hour resolution).**

Glacier forefield	Precipitation interval (mm)	No. events/total	No. events/year	No. events/total	No. events/year	No. events/total	No. events/year	Change from previous epoch	
Grastalferner		1954-1973 (epoch I)		1973-2006 (epoch II)		2006-2019 (epoch III)		I to II	II to III
(Horlachtal)	0 to 10	410	21.58	732	22.18	271	20.85	0.60	-1.34
	10 to 20	181	9.53	341	10.33	139	10.69	0.81	0.36
	20 to 30	113	5.95	191	5.79	70	5.38	-0.16	-0.40
	30 to 40	47	2.47	101	3.06	41	3.15	0.59	0.09
	40 to 50	26	1.37	35	1.06	9	0.69	-0.31	-0.37
	50 to 60	13	0.68	14	0.42	7	0.54	-0.26	0.11
	60 to 70	0	0.00	6	0.18	1	0.08	0.18	-0.10
	>70	2	0.11	0	0.00	1	0.08	-0.11	0.08
Gepatschferner		1953-1971 (epoch I)		1971-2006 (epoch II)		2006-2017 (epoch III)		I to II	II to III
(Kaunertal)	0 to 10	335	18.61	706	20.17	218	19.82	1.56	-0.35
	10 to 20	174	9.67	325	9.29	108	9.82	-0.38	0.53
	20 to 30	105	5.83	224	6.40	67	6.09	0.57	-0.31
	30 to 40	73	4.06	107	3.06	36	3.27	-1.00	0.22
	40 to 50	22	1.22	50	1.43	19	1.73	0.21	0.30
	50 to 60	11	0.61	19	0.54	4	0.36	-0.07	-0.18
	60 to 70	5	0.28	11	0.31	1	0.09	0.04	-0.22
	70 to 80	2	0.11	3	0.09	0	0.00	-0.03	-0.09
	80 to 90	0	0.00	2	0.06	0	0.00	0.06	-0.06
	90 to 100	0	0.00	5	0.14	2	0.18	0.14	0.04
	>100	4	0.22	5	0.14	0	0.00	-0.08	-0.14
Gepatschferner/ Müchner Abfahrt (Kaunertal)		1953-1971 (epoch I)		1971-2006 (epoch II)		2006-2017 (epoch III)		I to II	II to III
	0 to 10	304	16.89	618	17.66	202	18.36	0.77	0.71
	10 to 20	146	8.11	301	8.60	96	8.73	0.49	0.13
	20 to 30	101	5.61	197	5.63	64	5.82	0.02	0.19
	30 to 40	69	3.83	115	3.29	36	3.27	-0.55	-0.01
	40 to 50	35	1.94	50	1.43	21	1.91	-0.52	0.48
	50 to 60	12	0.67	26	0.74	6	0.55	0.08	-0.20
	60 to 70	5	0.28	12	0.34	1	0.09	0.07	-0.25
	70 to 80	1	0.06	5	0.14	0	0.00	0.09	-0.14
	>80	4	0.22	10	0.29	2	0.18	0.06	-0.10
Weißseeferner (Kaunertal)		1953-1971 (epoch I)		1971-2006 (epoch II)		2006-2017 (epoch III)		I to II	II to III
	0 to 10	302	16.78	623	17.80	212	19.27	1.02	1.47
	10 to 20	146	8.11	296	8.46	104	9.45	0.35	1.00
	20 to 30	99	5.50	203	5.80	60	5.45	0.30	-0.35
	30 to 40	75	4.17	104	2.97	34	3.09	-1.20	0.12
	40 to 50	32	1.78	46	1.31	19	1.73	-0.46	0.41
	50 to 60	12	0.67	28	0.80	6	0.55	0.13	-0.25
	60 to 70	3	0.17	14	0.40	1	0.09	0.23	-0.31
	70 to 80	1	0.06	3	0.09	1	0.09	0.03	0.01
	80 to 90	1	0.06	4	0.11	1	0.09	0.06	-0.02
	>90	3	0.17	6	0.17	0	0.00	0.00	-0.17
Hohenferner (Martelltal)		1959-2005 (epoch I)		2005-2019 (epoch II)		I to II			
	0 to 10	1169	25.41			387	27.64	2.23	
	10 to 20	403	8.76			127	9.07	0.31	
	20 to 30	241	5.24			50	3.57	-1.67	
	30 to 40	127	2.76			34	2.43	-0.33	
	40 to 50	54	1.17			18	1.29	0.11	



50 to 60	27	0.59	11	0.79	0.20
60 to 70	38	0.83	10	0.71	-0.11
70 to 80	16	0.35	4	0.29	-0.06
80 to 90	24	0.52	5	0.36	-0.16
90 to 100	5	0.11	3	0.21	0.11
100 to 110	5	0.11	1	0.07	-0.04
110 to 120	5	0.11	0	0.00	-0.11
120 to 130	4	0.09	1	0.07	-0.02
130 to 140	5	0.11	0	0.00	-0.11

675 Code availability

676 The processing of the historical aerial images into point clouds (and orthophotos) was done with the commercial software
 677 Agisoft Metashape Professional (Version 1.6.6). These point clouds as well as the point clouds based on LiDAR data (ALS)
 678 were further processed in the commercial geoinformation system SAGA LIS Pro 3D (Version 7.4.0) and converted into DEMs.
 679 The preparatory steps for the regression lines (derivation of the corresponding value pairs (SY and SCA)) were carried out in
 680 open-source software SAGA GIS (Version 7.2.0), whereby the subsequent automated repetition of the extraction of the value
 681 pairs by using a for-loop and the calculation of the corresponding regression lines were carried out in the open-source software
 682 R (RStudio, version 1.4.1103). Maps were created in both the open-source software SAGA GIS and QGIS (Version 3.22.4).
 683 Atmospheric simulation was performed using the Advanced Research version of the Weather Research and Forecasting
 684 (ARW-WRF) model (version 4.3). The meteorological analyses were carried out in R.

685 Data availability

686 The historical aerial images (HAI) and the corresponding calibration certificates (if available) were provided by the Federal
 687 Office of Metrology and Surveying (BEV, Vienna, Austria) (aerial image series 1953 and 1954), by the Italian Military
 688 Geographic Institute (IGMI, Florence, Italy) (aerial image series 1945 and 1959) and by the Province of Tyrol (aerial image
 689 series 1970, 1971 and 1973). The DEM 2006 (Horlachtal) and the point clouds of 2006 and 2004/2005 (Kaunertal and
 690 Martelltal) were provided by the Province of Tyrol and the Autonomous Province of Bolzano. The historical maps of
 691 1886/1887 (Kaunertal), 1889 (Horlachtal), 1918 (Martelltal) and 1922 (Kaunertal) were provided by the Archive of the German
 692 Alpine Club (DAV), the Ötztal Gedächtnisspeicher (Längenfeld, Austria), the BEV and the Bavarian Academy of Sciences
 693 and Humanities. The orthophotos of 2020 (all valleys) were made available for download by the Province of Tyrol and the
 694 Autonomous Province of Bolzano on their respective websites. The large-scale elevation data (DSM and Hillshade) (Overview
 695 Alps, Figure 1) was provided by Copernicus (Copernicus Land Monitoring Service). These data were produced with the
 696 financial support of the European Union. The 20th century NOAA/CIRES/DOE reanalysis data (V3) were provided by NOAA
 697 PSL, Boulder, Colorado, USA, from their website <https://psl.noaa.gov>. Support for the Twentieth Century Reanalysis Project
 698 version 3 dataset is provided by the U.S. Department of Energy, Office of Science Biological and Environmental Research
 699 (BER), by the National Oceanic and Atmospheric Administration Climate Program Office, and by the NOAA Earth System



700 Research Laboratory Physical Sciences Laboratory. Δ 8364; The ERA5 dataset we used is a Copernicus product. It contains
701 processed information from the Copernicus Climate Change Service [2021] and the Copernicus Atmosphere Monitoring
702 Service [2021]. Please note that neither the European Commission nor the European Centre for Medium-Range Weather
703 Forecasts is responsible for any use that may be made of the Copernicus information or data contained therein.

704 **Author contribution**

705 The study was conceptualised by MA, FH, TH and MB. Data preparation was carried out by MA, JR, FF, FH, LP, MP, MW,
706 LB, MS and SB-N. The methodological approach was developed by MA, JR, FH and TH for the SCA modelling and MA, FH
707 and MP for the meteorological analysis. The formal analysis was carried out by MA and MP. Supervision was carried out by
708 FH, TH and MB. The original draft was prepared by MA. JR, FF, FH, TH, LP, MP, MW, LB, MS, SB-N and MB were
709 involved in the revision of the manuscript. MB, FH and TH were responsible for fundraising and project management.

710 **Competing interests**

711 The authors declare that they have no conflict of interest.

712 **Acknowledgement**

713 We would like to thank the German Research Foundation (DFG), the Austrian Science Fund (FWF) and the Swiss National
714 Science Foundation (SNF) for financial support of the research project SEHAG (SENSitivity of High Alpine Geosystems to
715 climate change since 1850), within the framework of which this study was generated. Furthermore, we would like to thank for
716 providing the aerial images and the calibration certificates. In this context, we would like to thank the BEV, IGMI, the Province
717 of Tyrol, the Province of Bolzano and the Hydrographic Office of the Autonomous Province of Bolzano (Civil Protection
718 Agency). In addition, we would also like to thank the Province of Tyrol for providing the DEM 2006 (Horlachtal) as well as
719 the point cloud 2006 (Kaunertal) and the Autonomous Province of Bolzano for the point cloud 2006 (Martelltal). We would
720 also like to thank the Archive of the German Alpine Club (DAV), the Ötztaler Gedächtnisspeicher, the BEV and the Bavarian
721 Academy of Sciences and Humanities for providing the historical maps 1886/1887 (Kaunertal), 1889 (Horlachtal), 1918
722 (Martelltal) and 1922 (Kaunertal). We would also like to thank the Province of Tyrol and the Autonomous Province of Bolzano
723 for the orthophotos of 2020, which can be downloaded on their websites quickly and easily. We would also like to thank
724 Copernicus (Copernicus Land Monitoring Service) for the available download of the coarse resolution hillshade (Overview
725 Alps, Figure 1). Additionally, we would like to thank Wucher Helikopter GmbH (Ludesch, Austria) for carrying out the flights
726 in which the LiDAR data (ALS) 2017 (Kaunertal) and 2019 (Horlachtal and Martelltal) were acquired. Many thanks for the



727 safe flights even in difficult high alpine terrain. In addition, many thanks to NOAA PSL, Boulder, Colorado, USA for the
728 20CRv3 and Copernicus for the ERA5 dataset.

729 **Funding**

730 The study was financially supported by the German Research Foundation (DFG) and the Austrian Science Fund (FWF) (grant
731 numbers: BE 1118/38-1, BE 1118/39-1, BE 1118/40-1, HA 5740/10-1, HE 5747/6-1, MA 6966/4-1, LA 4426/1-1 and 4062-
732 N29). The open access publication of this article was supported by the Open Access Fund of the Catholic University of
733 Eichstätt-Ingolstadt.

734 **References**

- 735 Altmann, M., Piermattei, L., Haas, F., Heckmann, T., Fleischer, F., Rom, J., Betz-Nutz, S., Knoflach, B., Müller, S.,
736 Ramskogler, K., Pfeiffer, M., Hofmeister, F., Ressler, C., and Becht, M.: Long-Term Changes of Morphodynamics on
737 Little Ice Age Lateral Moraines and the Resulting Sediment Transfer into Mountain Streams in the Upper Kauner
738 Valley, Austria, *Water*, 12, 3375, <https://doi.org/10.3390/w12123375>, 2020.
- 739 Altmann, M., Haas, F., Heckmann, T., Liébault, F., and Becht, M.: Modelling of sediment supply from torrent catchments in
740 the Western Alps using the sediment contributing area (SCA) approach, *Earth Surf. Process. Landforms*, 46, 889–906,
741 <https://doi.org/10.1002/esp.5046>, 2021.
- 742 Anderson, S. W.: Uncertainty in quantitative analyses of topographic change: error propagation and the role of thresholding,
743 *Earth Surf. Process. Landforms*, 44, 1015–1033, <https://doi.org/10.1002/esp.4551>, 2019.
- 744 Bakker, M. and Lane, S.: Archival photogrammetric analysis of river-floodplain systems using Structure from Motion (SfM)
745 methods, *Earth Surf. Process. Landforms*, 42, 1274–1286, <https://doi.org/10.1002/esp.4085>, 2017.
- 746 Ballantyne, C. K.: A general model of paraglacial landscape response, *The Holocene*, 12, 371–376,
747 <https://doi.org/10.1191/0959683602hl553fa>, 2002a.
- 748 Ballantyne, C. K.: Paraglacial geomorphology, *Quaternary Science Reviews*, 21, 1935–2017, [https://doi.org/10.1016/S0277-3791\(02\)00005-7](https://doi.org/10.1016/S0277-3791(02)00005-7), 2002b.
- 750 Ballantyne, C. K. and Benn, D. I.: Paraglacial Slope Adjustment and Resedimentation following Recent Glacier Retreat,
751 Fåbergstølsdalen, Norway, *Arctic and Alpine Research*, 26, 255–269, 1994.
- 752 Becht, M.: Untersuchungen zur aktuellen Reliefentwicklung in alpinen Einzugsgebieten, Germany, Munich, 187 pp., 1995.
- 753 Beniston, M., Farinotti, D., Stoffel, M., Andreassen, L. M., Coppola, E., Eckert, N., Fantini, A., Giacomini, F., Hauck, C.,
754 Huss, M., Huwald, H., Lehning, M., López-Moreno, J.-I., Magnusson, J., Marty, C., Morán-Tejeda, E., Morin, S.,
755 Naaim, M., Provenzale, A., Rabatel, A., Six, D., Stötter, J., Strasser, U., Terzago, S., and Vincent, C.: The European



- 756 mountain cryosphere: a review of its current state, trends, and future challenges, *The Cryosphere*, 12, 759–794,
757 <https://doi.org/10.5194/tc-12-759-2018>, 2018.
- 758 Besl, P. J. and McKay, N. D.: Method for registration of 3-D shapes, in: *Sensor Fusion IV: Control Paradigms and Data*
759 *Structures*, Boston, MA, Friday 1 November 1991, 586–606, 1992.
- 760 Betz, S., Croce, V., and Becht, M.: Investigating morphodynamics on Little Ice Age lateral moraines in the Italian Alps
761 using archival aerial photogrammetry and airborne LiDAR data, *Zeitschrift für Geomorphologie*, 62, 231–247,
762 <https://doi.org/10.1127/zfg/2019/0629>, 2019.
- 763 Betz-Nutz, S.: Vergleichende photogrammetrische Untersuchungen zu langfristigen Veränderungen der Morphodynamik auf
764 neuzeitlichen Lateralmoränen ausgewählter Alpengletscher, Dissertation, Universitätsbibliothek Eichstätt-Ingolstadt,
765 Eichstätt, 2021.
- 766 Betz-Nutz, S., Heckmann, T., Haas, F., and Becht, M.: Development of the morphodynamics on LIA lateral moraines in ten
767 glacier forefields of the Eastern Alps since the 1950s, *Earth Surf. Dynam. Discuss.* [preprint],
768 <https://doi.org/10.5194/esurf-2022-24>, in review, 2022, 2022.
- 769 Blair, R. W.: Moraine and Valley Wall Collapse due to Rapid Deglaciation in Mount Cook National Park, New Zealand,
770 *Mountain Research and Development*, 14, 347, <https://doi.org/10.2307/3673731>, 1994.
- 771 Brugnara, Y., Brunetti, M., Maugeri, M., Nanni, T., and Simolo, C.: High-resolution analysis of daily precipitation trends in
772 the central Alps over the last century, *Int. J. Climatol.*, 32, 1406–1422, <https://doi.org/10.1002/joc.2363>, 2012.
- 773 Carrivick, J. L., Geilhausen, M., Warburton, J., Dickson, N. E., Carver, S. J., Evans, A. J., and Brown, L. E.: Contemporary
774 geomorphological activity throughout the proglacial area of an alpine catchment, *Geomorphology*, 188, 83–95,
775 <https://doi.org/10.1016/j.geomorph.2012.03.029>, 2013.
- 776 Cavalli, M., Goldin, B., Comiti, F., Brardinoni, F., and Marchi, L.: Assessment of erosion and deposition in steep mountain
777 basins by differencing sequential digital terrain models, *Geomorphology*, 291, 4–16,
778 <https://doi.org/10.1016/j.geomorph.2016.04.009>, 2017.
- 779 Chen, F. and Dudhia, J.: Coupling an Advanced Land Surface–Hydrology Model with the Penn State–NCAR MM5
780 Modeling System. Part II: preliminary model validation, *Mon. Wea. Rev.*, 129, 569–585, [https://doi.org/10.1175/1520-0493\(2001\)129<0569:CAALSH>2.0.CO;2](https://doi.org/10.1175/1520-0493(2001)129<0569:CAALSH>2.0.CO;2), 2001.
- 782 Church, M. and Ryder, J. M.: Paraglacial Sedimentation: A Consideration of Fluvial Processes Conditioned by Glaciation,
783 *Geol Soc America Bull*, 83, 3059, [https://doi.org/10.1130/0016-7606\(1972\)83\[3059:PSACOF\]2.0.CO;2](https://doi.org/10.1130/0016-7606(1972)83[3059:PSACOF]2.0.CO;2), 1972.
- 784 Cody, E., Anderson, B. M., McColl, S. T., Fuller, I. C., and Purdie, H. L.: Paraglacial adjustment of sediment slopes during
785 and immediately after glacial debuitressing, *Geomorphology*, 371, 107411,
786 <https://doi.org/10.1016/j.geomorph.2020.107411>, available at:
787 <https://www.sciencedirect.com/science/article/pii/S0169555X20303846>, 2020.
- 788 Conrad, O., Bechtel, B., Bock, M., Dietrich, H., Fischer, E., Gerlitz, L., Wehberg, J., Wichmann, V., and Böhner, J.: System
789 for Automated Geoscientific Analyses (SAGA) v. 2.1.4, *Geoscientific Model Development*, 8, 1991–2007, 2015.



- 790 Copernicus: Hillshade derived from EU-DEM version 1.0, [https://land.copernicus.eu/imagery-in-situ/eu-dem/eu-dem-v1-0-](https://land.copernicus.eu/imagery-in-situ/eu-dem/eu-dem-v1-0-and-derived-products/hillshade?tab=metadata)
791 [and-derived-products/hillshade?tab=metadata](https://land.copernicus.eu/imagery-in-situ/eu-dem/eu-dem-v1-0-and-derived-products/hillshade?tab=metadata), last access: 3 June 2021, 2016.
- 792 Curry, A. M., Cleasby, V., and Zukowskyj, P.: Paraglacial response of steep, sediment-mantled slopes to post-‘Little Ice
793 Age’ glacier recession in the central Swiss Alps, *J. Quaternary Sci.*, 21, 211–225, <https://doi.org/10.1002/jqs.954>, 2006.
- 794 Curry, A. M.: Paraglacial modification of slope form, *Earth Surf. Process. Landforms*, 24, 1213–1228,
795 [https://doi.org/10.1002/\(SICI\)1096-9837\(199912\)24:13<1213:AID-ESP32>3.0.CO;2-B](https://doi.org/10.1002/(SICI)1096-9837(199912)24:13<1213:AID-ESP32>3.0.CO;2-B), 1999.
- 796 Curry, A. M., Sands, T. B., and Porter, P. R.: Geotechnical controls on a steep lateral moraine undergoing paraglacial slope
797 adjustment, Geological Society, London, Special Publications, 320, 181–197, <https://doi.org/10.1144/SP320.12>, 2009.
- 798 Deline, P., Gruber, S., Delaloye, R., Fischer, L., Geertsema, M., Giardino, M., Hasler, A., Kirkbride, M., Krautblatter, M.,
799 Magnin, F., McColl, S., Ravel, L., and Schoeneich, P.: Ice Loss and Slope Stability in High-Mountain Regions, in:
800 Snow and ice-related hazards, risks, and disasters, edited by: Haeberli, W., Whiteman, C., and Shroder, J. F., Elsevier,
801 Amsterdam, 521–561, <https://doi.org/10.1016/B978-0-12-394849-6.00015-9>, 2015.
- 802 Draebing, D. and Eichel, J.: Spatial Controls of Turf-Banked Solifluction Lobes and Their Role for Paraglacial Adjustment
803 in Glacier Forelands, *Permafrost and Periglacial Processes*, 28, 446–459, <https://doi.org/10.1002/ppp.1930>, 2017.
- 804 Dusik, J.: Die aktuelle Geomorphodynamik auf proglazialen Moränen im Hinteren Kaunertal: Hochaufgelöste Messung und
805 Modellierung der Prozessdynamik hinsichtlich ihrer lokalen und temporalen Variabilität, Doctoral thesis, Physical
806 Geography, Catholic University of Eichstätt-Ingolstadt, Eichstätt, 2019.
- 807 Dusik, J.-M., Neugirg, F., and Haas, F.: Slope Wash, Gully Erosion and Debris Flows on Lateral Moraines in the Upper
808 Kaunertal, Austria, in: *Geomorphology of proglacial systems: Landform and sediment dynamics in recently deglaciated*
809 *alpine landscapes*, edited by: Heckmann, T. and Morche, D., Springer International Publishing, Cham, Switzerland, 177–
810 196, https://doi.org/10.1007/978-3-319-94184-4_11, 2019.
- 811 Eichel, J., Corenblit, D., and Dikau, R.: Conditions for feedbacks between geomorphic and vegetation dynamics on lateral
812 moraine slopes: a biogeomorphic feedback window, *Earth Surface Processes and Landforms*, 41, 406–419,
813 <https://doi.org/10.1002/esp.3859>, 2016.
- 814 Eltner, A., Kaiser, A., Castillo, C., Rock, G., Neugirg, F., and Abellán, A.: Image-based surface reconstruction in
815 geomorphometry – merits, limits and developments, *Earth Surf. Dynam.*, 4, 359–389, [https://doi.org/10.5194/esurf-4-](https://doi.org/10.5194/esurf-4-359-2016)
816 [359-2016](https://doi.org/10.5194/esurf-4-359-2016), 2016.
- 817 Finsterwalder, S.: Begleitworte zur Karte des Gepatschferners, *Zeitschrift für Gletscherkunde XVI (1/2)*, 20–41, 1928.
- 818 Finsterwalder, S. and Schunck, H.: Die Zunge des Gepatschferners 1886/87, *Zeitschrift des Deutschen und*
819 *Oesterreichischen Alpenvereins*, Tafel 4, 1888.
- 820 Fleischer, F., Haas, F., Piermattei, L., Pfeiffer, M., Heckmann, T., Altmann, M., Rom, J., Stark, M., Wimmer, H. W., Pfeifer,
821 N., and Becht, M.: Multi-decadal (1953–2017) rock glacier kinematics analysed by high-resolution topographic data in
822 the upper Kaunertal, Austria, *The Cryosphere*, 15, 5345–5369, <https://doi.org/10.5194/tc-15-5345-2021>, 2021.



- 823 Fryirs, K.: (Dis)Connectivity in catchment sediment cascades: a fresh look at the sediment delivery problem, *Earth Surf.*
824 *Process. Landforms*, 38, 30–46, <https://doi.org/10.1002/esp.3242>, 2013.
- 825 Fryirs, K. A., Brierley, G. J., Preston, N. J., and Spencer, J.: Catchment-scale (dis)connectivity in sediment flux in the upper
826 Hunter catchment, New South Wales, Australia, *Geomorphology*, 84, 297–316,
827 <https://doi.org/10.1016/j.geomorph.2006.01.044>, 2007.
- 828 Geitner, C.: Sedimentologische und vegetationsgeschichtliche Untersuchungen an fluvialen Sedimenten in den Hochlagen
829 des Horlachteles (Stubai Alpen, Tirol): ein Beitrag zur zeitlichen Differenzierung der fluvialen Dynamik im Holozän,
830 vol. 31 of *Münchener Geographische Abhandlungen A*, Geobuch-Verlag, Diss., München, 1999.
- 831 Geological Survey of Austria: Geological map of Austria, 1:2.000.000, Vienna, 1999.
- 832 Glira, P., Pfeifer, N., Briese, C., and Ressler, C.: A Correspondence Framework for ALS Strip Adjustments based on Variants
833 of the ICP Algorithm, 275–289, <https://doi.org/10.1127/PFG/2015/0270>, 2015.
- 834 Gomez, C., Hayakawa, Y., and Obanawa, H.: A study of Japanese landscapes using structure from motion derived DSMs
835 and DEMs based on historical aerial photographs: New opportunities for vegetation monitoring and diachronic
836 geomorphology, *Geomorphology*, 242, 11–20, <https://doi.org/10.1016/j.geomorph.2015.02.021>, 2015.
- 837 Groß, G. and Patzelt, G.: The Austrian Glacier Inventory for the Little Ice Age Maximum (GI LIA) in ArcGIS (shapefile)
838 format, 2015.
- 839 Haas, F.: Fluviale Hangprozesse in alpinen Einzugsgebieten der nördlichen Kalkalpen: Quantifizierung und
840 Modellierungsansätze, Doctoral thesis, Munich, Catholic University of Eichstätt-Ingolstadt, 2008.
- 841 Haas, F., Heckmann, T., Hilger, L., and Becht, M.: Quantification and Modelling of Debris Flows in the Proglacial Area of
842 the Gepatschferner/Austria using Ground-based LIDAR, Collins, Adrian L. ; Golosov, Valentin ; Horowitz, Arthur J. ;
843 Lu, Xixi ; Stone, Mike ; Walling, Des E. ; Zhang, Xinbao (Eds.): *Erosion and Sediment Yields in the Changing*
844 *Environment: proceedings of an IAHS International Commission on Continental Erosion Symposium, held at the*
845 *Institute of Mountain Hazards and Environment, CAS-Chengdu, China, 11-15 October 2012, IAHS publication*, 356,
846 293–302, 2012.
- 847 Haas, F., Heckmann, T., Wichmann, V., and Becht, M.: Quantification and Modeling of Fluvial Bedload Discharge from
848 Hillslope Channels in two Alpine Catchments (Bavarian Alps, Germany), *Zeitschrift für Geomorphologie N.F. Suppl.*,
849 55, 147–168, <https://doi.org/10.1127/0372-8854/2011/0055S3-0056>, 2011.
- 850 Haeberli, W. and Whiteman, C.: *Snow and Ice-Related Hazards, Risks, and Disasters*, Elsevier, 2021.
- 851 Hagg, W. and Becht, M.: Einflüsse von Niederschlag und Substrat auf die Auslösung von Hangmuren in Beispielgebieten
852 der Ostalpen, *Zeitschrift für Geomorphologie*, 79–92, 2000.
- 853 Haselberger, S., Zangerl, U., Scheper, S., Otto, J.-C., Ohler, L.-M., Junker, R. R., and Kraushaar, S.: Catchment-Scale
854 Stability and Disturbance in Biogeomorphic Succession in an Alpine Glacier Foreland (Kautertal Valley, Austria),
855 *SSRN Journal*, <https://doi.org/10.2139/ssrn.4202209>, 2022.



- 856 Haselberger, S., Ohler, L.-M., Junker, R. R., Otto, J.-C., Glade, T., and Kraushaar, S.: Quantification of biogeomorphic
857 interactions between small-scale sediment transport and primary vegetation succession on proglacial slopes of the
858 Gepatschferner, Austria, *Earth Surf. Process. Landforms*, 46, 1941–1952, <https://doi.org/10.1002/esp.5136>, 2021.
- 859 Heckmann, T. and Morche, D. (Eds.): *Geomorphology of proglacial systems: Landform and sediment dynamics in recently*
860 *deglaciated alpine landscapes*, *Geography of the Physical Environment*, Springer International Publishing, Cham,
861 Switzerland, 2019.
- 862 Heckmann, T. and Vericat, D.: Computing spatially distributed sediment delivery ratios: inferring functional sediment
863 connectivity from repeat high-resolution digital elevation models, *Earth Surf. Process. Landforms*, 43, 1547–1554,
864 <https://doi.org/10.1002/esp.4334>, 2018.
- 865 Heinimann, H., Hollenstein, K., Kienholz, H., Krummenacher, B., and Mani, P.: *Methoden zur Analyse und Bewertung von*
866 *Naturgefahren*, 85, *Umwelt-Materialien*, BUWAL - Bundesamt für Umwelt, Wald und Landschaft, Bern, 1998.
- 867 Hilger, L.: *Quantification and regionalization of geomorphic processes using spatial models and high-resolution topographic*
868 *data: A sediment budget of the Upper Kauner Valley, Ötztal Alps*, Doctoral thesis, *Physical Geography*, Catholic
869 University of Eichstätt-Ingolstadt, Eichstätt, 2017.
- 870 Hock, R., Rasul, G., Adler, C., Cáceres, B., Gruber, S., Hirabayashi, Y., Jackson, M., Kääb, A., Kang, S., Kutuzov, S., and
871 Milner, A. L.: High Mountain Areas: In: *IPCC Special Report on the Ocean and Cryosphere in a Changing Climate* [H.-
872 O. Pörtner, D.C. Roberts, V. Masson-Delmotte, P. Zhai, M. Tignor, E. Poloczanska, K. Mintenbeck, A. Alegría, M.
873 Nicolai, A. Okem, J. Petzold, B. Rama, N.M. Weyer (eds.)]. Cambridge University Press, Cambridge, UK and New
874 York, NY, USA, 131–202, <https://doi.org/10.1017/9781009157964.004>, 2019.
- 875 Hodgson, M. E. and Bresnahan, P.: Accuracy of Airborne Lidar-Derived Elevation, <https://doi.org/10.14358/PERS.70.3.331>,
876 2004.
- 877 Hong, S. Y., Noh, Y., and Dudhia, J.: A new vertical diffusion package with an explicit treatment of entrainment processes,
878 *Mon. Weather Rev.*, 134, 2318–2341, <https://doi.org/10.1175/MWR3199.1>, 2006.
- 879 Huber, A., Heckmann, T., Haas, F., and Becht, M.: DEM-based scaling of bedload sediment yield in low-order torrents of
880 the Isar catchment, In: *Guidelines for Assessing Sediment Dynamics in Alpine Basins and Channel Reaches: Final*
881 *Report of the SedAlp Project*, Work Package 4. SedAlp, Vienna; Annex 39-46, 2015.
- 882 Hugenholtz, C. H., Moorman, B. J., Barlow, J., and Wainstein, P. A.: Large-scale moraine deformation at the Athabasca
883 Glacier, Jasper National Park, Alberta, Canada, *Landslides*, 5, 251–260, <https://doi.org/10.1007/s10346-008-0116-5>,
884 2008.
- 885 Iacono, M. J., Delamere, J. S., Mlawer, E. J., Shephard, M. W., Clough, S. A., and Collins, W. D.: Radiative forcing by long-
886 lived greenhouse gases: Calculations with the AER radiative transfer models, *J. Geophys. Res.*, 113,
887 <https://doi.org/10.1029/2008JD009944>, 2008.
- 888 IPCC: *Climate Change 2021: The Physical Science Basis. Contribution of Working Group I to the Sixth Assessment Report*
889 *of the Intergovernmental Panel on Climate Change* [Masson-Delmotte, V., P. Zhai, A. Pirani, S.L. Connors, C. Péan, S.



- 890 Berger, N. Caud, Y. Chen, L. Goldfarb, M.I. Gomis, M. Huang, K. Leitzell, E. Lonnoy, J.B.R. Matthews, T.K.
891 Maycock, T. Waterfield, O. Yelekçi, R. Yu, and B. Zhou (eds.)], Cambridge University Press. In Press, 2021.
- 892 Jiménez, P. A., Dudhia, J., González-Rouco, J. F., Navarro, J., Montávez, J. P., and García-Bustamante, E.: A Revised
893 Scheme for the WRF Surface Layer Formulation, *Mon. Wea. Rev.*, 140, 898–918, <https://doi.org/10.1175/mwr-d-11->
894 00056.1, 2012.
- 895 Kain, J. S.: The Kain–Fritsch Convective Parameterization: An Update, *Journal of Applied Meteorology and Climatology*,
896 43, 170–181, [https://doi.org/10.1175/1520-0450\(2004\)043<0170:TKCPAU>2.0.CO;2](https://doi.org/10.1175/1520-0450(2004)043<0170:TKCPAU>2.0.CO;2), available at:
897 https://journals.ametsoc.org/view/journals/apme/43/1/1520-0450_2004_043_0170_tkcpau_2.0.co_2.xml, 2004.
- 898 Klein, G., Vitasse, Y., Rixen, C., Marty, C., and Rebetez, M.: Shorter snow cover duration since 1970 in the Swiss Alps due
899 to earlier snowmelt more than to later snow onset, *Climatic Change*, 139, 637–649, <https://doi.org/10.1007/s10584-016->
900 1806-y, 2016.
- 901 Lane, S., Bakker, M., Gabbud, C., Micheletti, N., and Saugy, J.-N.: Sediment export, transient landscape response and
902 catchment-scale connectivity following rapid climate warming and Alpine glacier recession, *Geomorphology*, 277, 210–
903 227, <https://doi.org/10.1016/j.geomorph.2016.02.015>, available at: <http://dx.doi.org/10.1016/j.geomorph.2016.02.015>,
904 2017.
- 905 Lane, S. N., Westaway, R. M., and Murray Hicks, D.: Estimation of erosion and deposition volumes in a large, gravel-bed,
906 braided river using synoptic remote sensing, *Earth Surf. Process. Landforms*, 28, 249–271,
907 <https://doi.org/10.1002/esp.483>, 2003.
- 908 Mair, V. and Purtscheller, F.: *Exkursion E: Geologie und Petrologie des Ortlerkristallins*, *Mitteilungen der Österreichischen*
909 *Mineralogischen Gesellschaft*, 285–303, 1996.
- 910 Mair, V., Nocker, C., and Tropper, P.: *Das Ortler-Campo Kristallin in Südtirol*, *Mitteilungen der Österreichischen*
911 *Mineralogischen Gesellschaft*, 219–240, 2007.
- 912 Mankin, J. S. and Diffenbaugh, N. S.: Influence of temperature and precipitation variability on near-term snow trends, *Clim*
913 *Dyn*, 45, 1099–1116, <https://doi.org/10.1007/s00382-014-2357-4>, 2015.
- 914 Mattson, L. E. and Gardner, J. S.: Mass Wasting on Valley-Side Ice-Cored Moraines, *Boundary Glacier, Alberta, Canada*,
915 *Geografiska Annaler: Series A, Physical Geography*, 73, 123–128, <https://doi.org/10.1080/04353676.1991.11880337>,
916 1991.
- 917 Midgley, N. G. and Tonkin, T. N.: Reconstruction of former glacier surface topography from archive oblique aerial images,
918 *Geomorphology*, 282, 18–26, <https://doi.org/10.1016/j.geomorph.2017.01.008>, 2017.
- 919 Mölg, N. and Bolch, T.: Structure-from-Motion Using Historical Aerial Images to Analyse Changes in Glacier Surface
920 Elevation, *Remote Sensing*, 9, 1021, <https://doi.org/10.3390/rs9101021>, available at: <https://www.mdpi.com/228032>,
921 2017.
- 922 Morrison, H., Thompson, G., and Tatarskii, V.: Impact of Cloud Microphysics on the Development of Trailing Stratiform
923 Precipitation in a Simulated Squall Line: Comparison of One- and Two-Moment Schemes, *Mon. Wea. Rev.*, 137, 991–



- 924 1007, <https://doi.org/10.1175/2008MWR2556.1>, available at:
925 https://journals.ametsoc.org/view/journals/mwre/137/3/2008mwr2556.1.xml?tab_body=pdf, 2009.
- 926 Nebiker, S., Lack, N., and Deuber, M.: Building Change Detection from Historical Aerial Photographs Using Dense Image
927 Matching and Object-Based Image Analysis, *Remote Sensing*, 6, 8310–8336, <https://doi.org/10.3390/rs6098310>, 2014.
- 928 Neugirg, F., Kaiser, A., Huber, A., Heckmann, T., Schindewolf, M., Schmidt, J., Becht, M., and Haas, F.: Using terrestrial
929 LiDAR data to analyse morphodynamics on steep unvegetated slopes driven by different geomorphic processes,
930 *CATENA*, 142, 269–280, <https://doi.org/10.1016/j.catena.2016.03.021>, 2016.
- 931 Neugirg, F., Kaiser, A., Schmidt, J., Becht, M., and Haas, F.: Quantification, analysis and modelling of soil erosion on steep
932 slopes using LiDAR and UAV photographs, *Proc. IAHS*, 367, 51–58, 2015a.
- 933 Neugirg, F., Kaiser, A., Schindewolf, M., Becht, M., Schmidt, J., and Haas, F.: Monitoring and modeling slope dynamics in
934 an Alpine watershed - a combined approach of soil science remote sensing and geomorphology, *Proc. IAHS*, 371, 181–
935 187, 2015b.
- 936 O'Callaghan, J. F. and Mark, D. M.: The extraction of drainage networks from digital elevation data. *Computer vision,*
937 *graphics, and image processing*, 28, 323–344, 1984.
- 938 Okay, U., Telling, J., Glennie, C. L., and Dietrich, W. E.: Airborne lidar change detection: An overview of Earth sciences
939 applications, *Earth-Science Reviews*, 198, 102929, <https://doi.org/10.1016/j.earscirev.2019.102929>, 2019.
- 940 Pelletier, J. D. and Orem, C. A.: How do sediment yields from post-wildfire debris-laden flows depend on terrain slope, soil
941 burn severity class, and drainage basin area? Insights from airborne-LiDAR change detection, *Earth Surf. Process.*
942 *Landforms*, 39, 1822–1832, <https://doi.org/10.1002/esp.3570>, 2014.
- 943 Pepin, N. C., Arnone, E., Gobiet, A., Haslinger, K., Kotlarski, S., Notarnicola, C., Palazzi, E., Seibert, P., Serafin, S.,
944 Schöner, W., Terzago, S., Thornton, J. M., Vuille, M., and Adler, C.: Climate Changes and Their Elevational Patterns in
945 the Mountains of the World, *Reviews of Geophysics*, 60, e2020RG000730, <https://doi.org/10.1029/2020RG000730>,
946 2022.
- 947 Pfeifer, N., Mandlbürger, G., Otepka, J., and Karel, W.: OPALS – A framework for Airborne Laser Scanning data analysis,
948 *Computers, Environment and Urban Systems*, 45, 125–136, <https://doi.org/10.1016/j.compenvurbsys.2013.11.002>,
949 available at: <http://dx.doi.org/10.1016/j.compenvurbsys.2013.11.002>, 2014.
- 950 Piermattei, L., Heckmann, T., Betz-Nutz, S., Altmann, M., Rom, J., Fleischer, F., Stark, M., Haas, F., Ressler, C., Wimmer,
951 M., Pfeifer, N., and Becht, M.: Evolution of an Alpine proglacial river during seven decades of deglaciation quantified
952 from photogrammetric and LiDAR digital elevation models, *Earth Surf. Dynam. Discuss.* [preprint],
953 <https://doi.org/10.5194/esurf-2022-63>, 2022.
- 954 Pulighe, G. and Fava, F.: DEM extraction from archive aerial photos: accuracy assessment in areas of complex topography,
955 *European Journal of Remote Sensing*, 46, 363–378, <https://doi.org/10.5721/EuJRS20134621>, 2013.
- 956 Rieger, D.: Bewertung der naturräumlichen Rahmenbedingungen für die Entstehung von Hangmuren: Möglichkeiten zur
957 Modellierung des Murpotentials, vol. 51 of *Münchener Geographische Abhandlungen A*, Geobuch, München, 1999.



- 958 Rolstad, C., Haug, T., and Denby, B.: Spatially integrated geodetic glacier mass balance and its uncertainty based on
959 geostatistical analysis: application to the western Svartisen ice cap, Norway, *J. Glaciol.*, 55, 666–680,
960 <https://doi.org/10.3189/002214309789470950>, 2009.
- 961 Sass, O., Haas, F., Schimmer, C., Heel, M., Bremer, M., Stöger, F., and Wetzel, K.: Impact of forest fires on geomorphic
962 processes in the tyrolean limestone alps, *Geografiska Annaler: Series A, Physical Geography*, 94, 117–133,
963 <https://doi.org/10.1111/j.1468-0459.2012.00452.x>, 2012.
- 964 Schiefer, E. and Gilbert, R.: Reconstructing morphometric change in a proglacial landscape using historical aerial
965 photography and automated DEM generation, *Geomorphology*, 88, 167–178,
966 <https://doi.org/10.1016/j.geomorph.2006.11.003>, 2007.
- 967 Serquet, G., Marty, C., Dulex, J.-P., and Rebetez, M.: Seasonal trends and temperature dependence of the
968 snowfall/precipitationday ratio in Switzerland, *Geophys. Res. Lett.*, 38, 14–18, <https://doi.org/10.1029/2011GL046976>,
969 2011.
- 970 Sevara, C., Verhoeven, G., Doneus, M., and Draganits, E.: Surfaces from the Visual Past: Recovering High-Resolution
971 Terrain Data from Historic Aerial Imagery for Multitemporal Landscape Analysis, *J Archaeol Method Theory*, 25, 611–
972 642, <https://doi.org/10.1007/s10816-017-9348-9>, available at: <https://link.springer.com/article/10.1007/s10816-017-9348-9>, 2018.
- 973
- 974 Smith, M. W., Carrivick, J. L., and Quincey, D. J.: Structure from motion photogrammetry in physical geography, *Progress*
975 *in Physical Geography: Earth and Environment*, 40, 247–275, <https://doi.org/10.1177/0309133315615805>, 2016.
- 976 Staindl, A.: *Kurze Geologie von Südtirol*, Weger, Brixen, 2000.
- 977 Stark, M., Rom, J., Haas, F., Piermattei, L., Fleischer, F., Altmann, M., and Becht, M.: Long-term assessment of terrain
978 changes and calculation of erosion rates in an alpine catchment based on SfM-MVS processing of historical aerial
979 images. How camera information and processing strategy affect quantitative analysis, *jgeomorphology*,
980 <https://doi.org/10.1127/jgeomorphology/2022/0755>, 2022.
- 981 Tarolli, P.: High-resolution topography for understanding Earth surface processes: Opportunities and challenges,
982 *Geomorphology*, 216, 295–312, <https://doi.org/10.1016/j.geomorph.2014.03.008>, 2014.
- 983 Tollmann, A.: *Geologie von Österreich: Die Zentralalpen*, Deuticke, Wien, 1977.
- 984 Vehling, L.: *Gravitative Massenbewegungen an alpinen Felshängen: Quantitative Bedeutung in der Sedimentkaskade*
985 *proglazialer Geosysteme (Kaunertal, Tirol)*, Doctoral thesis, Friedrich-Alexander-Universität Erlangen-Nürnberg,
986 Erlangen, 2016.
- 987 Veit, H.: *Die Alpen: Geoökologie und Landschaftsentwicklung*, Ulmer, Stuttgart, 2002.
- 988 Wester, T., Wasklewicz, T., and Staley, D.: Functional and structural connectivity within a recently burned drainage basin,
989 *Geomorphology*, 206, 362–373, <https://doi.org/10.1016/j.geomorph.2013.10.011>, available at:
990 <http://www.sciencedirect.com/science/article/pii/S0169555X13005242>, 2014.



991 Zhong, Y., Liu, Q., Westoby, M., Nie, Y., Pellicciotti, F., Zhang, B., Cai, J., Liu, G., Liao, H., and Lu, X.: Intensified
992 paraglacial slope failures due to accelerating downwasting of a temperate glacier in Mt. Gongga, southeastern Tibetan
993 Plateau, *Earth Surf. Dynam.*, 10, 23–42, <https://doi.org/10.5194/esurf-10-23-2022>, 2022.
994